Solution-Processed Tin-Based Perovskite for Near Infrared Lasing

Xing, Guichuan; Kumar, Mulmudi Hemant; Chong, Wee Kiang; Liu, Xinfeng; Cai, Yao; Ding, Hong; Asta, Mark; Grätzel, Michael; Mhaisalkar, Subodh; Mathews, Nripan; Sum, Tze Chien

Solution-Processed Tin-Based Perovskite for Near Infrared Lasing

By Guichuan Xing, Mulmudi Hemant Kumar, Wee Kiang Chong, Xinfeng Liu,
Yao Cai, Hong Ding, Mark Asta, Michael Grätzel, Subodh Mhaisalkar,
Nripan Mathews*, and Tze Chien Sum*

((Optional Dedication))

[*] Dr. G. Xing, W. K. Chong, Dr. X. Liu, Prof. T. C. Sum
Division of Physics and Applied Physics, School of Physical and Mathematical Sciences
Nanyang Technological University, 21 Nanyang Link, 637371 (Singapore)
E-mail: Tzechien@ntu.edu.sg
        Dr. M. H. Kumar, Prof. S. Mhaisalkar, Prof. N. Mathews
Energy Research Institute @NTU (ERI@N), Research Techno Plaza, X-Frontier Block, Level 5, 50 Nanyang Drive, 637553 (Singapore)
School of Materials Science and Engineering, Nanyang Technological University, Nanyang Avenue, 639798 (Singapore)
E-mail: Nripan@ntu.edu.sg
        Y. Cai, Dr. H. Ding, Prof. M. Asta
Department of Materials Science and Engineering, University of California, Berkeley, CA 94720 (USA)
        Prof. M. Grätzel
Energy Research Institute @NTU (ERI@N), Research Techno Plaza, X-Frontier Block, Level 5, 50 Nanyang Drive, 637553 (Singapore)
Laboratory of Photonics and Interfaces, Department of Chemistry and Chemical Engineering, Swiss Federal Institute of Technology, Station 6, CH-1015 Lausanne, Switzerland.
        Dr. M. H. Kumar
Present address: Research School of Engineering, The Australian National University, Canberra, Australia 2601
        Dr. X. Liu
Present address: CAS Center for Excellence in Nanoscience & CAS Key Laboratory of Standardization and Measurement for Nanotechnology, National Center for Nanoscience and Technology, Beijing 100190, China

Coherent near-infrared (NIR) light sources play a pivotal role in optoelectronics, telecommunications and imaging applications.[1-13] The development of an effective on-chip laser holds the key to the true integration of optical and electrical circuitry on the ubiquitous Si platform. The low radiative recombination rate associated with Si's indirect energy bandgap compels the integration of high quality semiconductor thin films (*e.g.*, gallium arsenide (GaAs) and indium gallium nitride (InGaN) as the NIR gain media. However, their integration onto the Si platform is hampered by lattice mismatch, thereby necessitating complex approaches such as metamorphic buffer layers and wafer bonding.[1-7] Hence, there is a need for facile, low-temperature solution processed gain materials that would not only reduce the production costs but would also be amenable to a much wider range of resonator designs on non-conformal/flexible substrates. However, choices are limited as narrow bandgap materials (such as organic semiconductors and colloidal quantum dots) face inherent challenges from fast non-radiative recombination and significant Auger losses.[7-14]

Solution-processed $CH_3NH_3PbX_3$ (where X=Cl, Br, I) with their outstanding optoelectronic properties of large absorption coefficient, low trap density, long balanced charge diffusion lengths, and slow bimolecular recombination, have recently demonstrated great potential for both light harvesting[15-21] and light emission applications[22-26]. Record photovoltaic efficiencies exceeding 20% have been achieved with these cells.[21] Low threshold amplified spontaneous emission (ASE) and high Q lasing from 400 nm to 800 nm have been demonstrated with lead halide perovskite thin films and micro/nano-structures, respectively.[22-24] The peak external quantum efficiency (EQE) of light emitting diodes built from these perovskites have quickly jumped from less than 1% in 2014[25] to ~8% in 2015[26]. However, such perovskites are still limited to the same lead-based ones where toxicity concerns have stifled their commercial aspirations. The emission wavelength of $CH_3NH_3PbX_3$ tunable up to around 780 nm also limits their near infrared applications. Furthermore, the

slow bimolecular recombination in lead-based perovskites[18] that spurs efficient photovoltaic operation is a fundamental limitation towards improving the light emitting properties.

Herein, we reveal that solution-processed lead-free tin-based halide perovskites ($CsSnX_3$, X = Br, I) despite exhibiting very poor photovoltaic performance,[27-33] surprisingly possesses exceptional optical gain properties in the NIR up to ~1 μm – wavelengths unattainable by the leaded $CH_3NH_3PbX_3$. Ultralow threshold (~6 μJ/cm^2), large gain (200 cm^{-1}) stimulated emission from 20% SnF_2-added $CsSnI_3$ samples is demonstrated, which are comparable to their leaded counterparts.[22-24] NIR lasing (Q~500) is achieved using the natural photonic crystal corrugations in the scales of a butterfly wing. Transient spectroscopy provides direct evidence that SnF_2-addition effectively suppresses the trap states in $CsSnI_3$ and the lasing originates from the free electron-hole bimolecular recombination with a high rate of ~10^{-8} cm^3s^{-1} (i.e., 1-2 orders larger than $CH_3NH_3PbI_3$). Room-temperature, ultrastable (>20 hours), NIR coherent light emission (700-1000 nm) can be achieved with judicious substitution. Importantly, these solution-processable Pb-free perovskites present a substrate-insensitive infrared wavelength tunable lasing solution for applications in non-conformal, non-planar geometries or flexible substrates. This tin-based perovskite is a new model system for perovskite light emission applications.

The samples of $CsSnI_3$ are spin-coated and dried at $100^{°}C$. They display a perovskite structure (**Figure 1**a) with an orthorhombic phase (Figure S1 - S3), exhibiting ~1.3 eV (950 nm) emission from direct bandgap transitions (Figure 1b). With increasing photoexcitation fluence, the emission from the SnF_2-added $CsSnI_3$ films (*i.e.*, 5%, 10%, 20% mol concentration) undergo a transition from spontaneous emission (SE) to amplified spontaneous emission (ASE), exhibiting a clear reduction in the FWHM- Figure 1b, 1c. Above the threshold pump fluence (F_{Thr}), the emission intensity increases superlinearly with increasing pump fluence (Figure 1c). Correspondingly, above F_{Thr} (Figure S4 & S5), the PL decay transients also show a clear switch from SE (~110 ps – dominated by the multiparticle interaction) to ASE (<10 ps

– dominated by the photon avalanche and limited by the streak camera's temporal response). These are clear signatures of optical gain from SnF_2-added $CsSnI_3$ films. Figure 1c & S5 show that with increasing SnF_2 addition (to ≤ 20%), F_{Thr} decreases progressively with values of 16 ± 2, 7 ± 1, 6 ± 1 $\mu J/cm^2$ for the 5%, 10% and 20% SnF_2-added $CsSnI_3$ films, respectively. However, SE merely increases continually with increasing pump fluence in the untreated $CsSnI_3$ film, without achieving population inversion within the limits of its damage threshold. Any further increase of SnF_2 concentration to beyond the optimal 20% led to a rise in F_{Thr} instead (*e.g.*, up to 18 $\mu J/cm^2$ for 30%). The F_{Thr} of 20% SnF_2-treated $CsSnI_3$ film is comparable to that reported for $CH_3NH_3PbI_3$ (~12 $\mu J/cm^2$) under the same experimental conditions.[22] This ultralow threshold of 6 ± 1 $\mu J/cm^2$ is among the lowest reported values for solution-processed organic or inorganic thin films (typically ≥ 5 $\mu J/cm^2$ without any optical feedback cavities).[7-13,24] Furthermore, PLQY as large as $13 \pm 1\%$ is measured for the 20% SnF_2-treated $CsSnI_3$ film, which is again comparable for the leaded $CH_3NH_3PbI_3$ system (~17%) (Figure S6a).[22] Variable stripe length (VSL) measurements revealed gains of 120 ± 10, 130 ± 10 and 200 ± 10 cm^{-1} for the 5%, 10% and 20% SnF_2-treated $CsSnI_3$ films, respectively (Figure S6b). Comparatively, the gain of the 20% SnF_2-treated $CsSnI_3$ films is comparable with the leaded $CH_3NH_3PbI_3$ film (40 ± 10 cm^{-1})[22] and $CsPbI_3$ nanocrystal film (450 ± 10 cm^{-1})[24]; and is better than conjugated polymer thin films (0.92 - 154 cm^{-1})[7-10] and traditional colloidal nanocrystals (60 - 95 cm^{-1})[13]. These results clearly show that the SnF_2-treated $CsSnI_3$ lead-free perovskite is a very promising NIR gain medium.

To demonstrate the outstanding intrinsic NIR lasing properties of $CsSnI_3$ in a non-conformal and non-planar substrate, we drop-casted 20% SnF_2-treated $CsSnI_3$ on a butterfly wing (genus: *delias hyparete metarete*). Another reason for choosing the imperfect natural cavity is that it is readily available and is of much lower costs compared to traditional micro- to nano-optical cavities fabricated with carefully designed lithographic procedures. Figure 1d shows a close up optical image of the scales on the wing. Each scale (~100 μm × 80 μm) possesses

4

near periodic and parallel corrugations (or lamella) with almost identical interspacing, supported by cross-ribs – Figure 1e. Effectively, these scales form natural photonic crystals that reflect different colours depending on the lamella interspacing. Here, we had utilized the white part of the butterfly wing (Figure 1d inset) whose scales have a lamella interspacing of ~2 μm, which could provide the cavity resonance close to the emission peak of $CsSnI_3$ (Figure S9d). SEM imaging showed that the perovskite can infiltrate well into the butterfly wing (Figure S7). Single-mode, low threshold lasing (~15 μJ/cm^2) from the embedded $CsSnI_3$ (20% SnF_2) gain medium was achieved – Figure 1f and S8. Our lasing experiments correspond well with the results obtained from modelling the cavity mode and the optical feedback mechanism (Figure 1e and S9). The laser line exhibits a FWHM of ~1.9 nm (limited by the resolution of spectrometer) with a relatively high Q factor (*i.e.*, Q = $\lambda/\Delta\lambda$ ≥500, where λ and $\Delta\lambda$ are the wavelength and the FWHM of the laser emission). Despite the imperfectness of a natural photonic crystal cavity (Figure 1e), this Q value compares favorably with typical value (~ 200) from lithographically-patterned gratings.[8] Single mode lasing above 1 μm could also be achieved at different locations of the wing with different lamella interspacing - Figure S10.

The question on whether the gain mechanism in these $CsSnI_3$ films originates from excitonic or electron-hole plasma recombination has important ramifications on the laser architecture design. Presently, the origin of the $CsSnI_3$ band edge emission from excitonic recombination or free carrier recombination is still a matter of debate.[29,30] Through detailed transient PL, we determined that the free carrier mechanism dominates the emission from these Pb-free perovskite gain medium. **Figure 2**a shows the pump fluence dependent PL decay transients of 20% SnF_2-treated $CsSnI_3$ monitored over the entire band edge emission range. Below ~0.6 μJ/cm^2, the PL dynamics display a near mono-exponential slower decay profile. Above ~0.6 μJ/cm^2, a fast non-exponential decay component appears. Figure 2b summarizes the initial time PL intensity ($I_{PL}[t = 0]$) and effective PL lifetime as a function of pump fluence for both

the 0% and 20% SnF_2-added films. $I_{PL}[t = 0]$ shows a clear transition from linear to quadratic

behavior at a fluence of ~0.6 $\mu J/cm^2$ for the 20% SnF_2- treated film (Figure 2b, upper panel).

The linear behavior indicates that the PL is dominated by trap-assisted recombination at low

pump fluence; while the quadratic behavior clearly shows that the PL originates from the

bimolecular recombination between free carriers at higher pump fluence.[18,34] In contrast, the

untreated $CsSnI_3$ film only showed a linear dependence throughout, indicating a much higher

trap density. Based on the bimolecular signature, one should expect an increased

recombination rate with increasing carrier concentrations at higher pump fluence. Indeed, this

behavior is evident from Figure 2b (lower panel) for the 20% SnF_2-treated film, where an

inverse relation between the effective PL lifetime (defined as $I_{PL}(t)= I_{PL}[t = 0]/e$) and the

pump fluence (at >0.6 $\mu J/cm^2$) is obtained. On the other hand, $I_{PL}[t = 0]$ is linearly dependent

on the pump fluence and possesses a near invariant effective PL lifetime (Figure 2b) at pump

fluence below 0.6 $\mu J/cm^2$. Our findings on the free-carrier nature of the recombination are

consistent with the small exciton binding energy (0.1 - 18 meV) reported for $CsSnI_3$.[30] Free

electron-hole recombination rate decreases with increasing temperature. The PL lifetime

lengthening (Figure S19) and increasing ASE threshold (Figure S20) with temperature in the

optimized film also further validates the free electron-hole recombination. Through fitting the

pump fluence dependent time-resolved photoluminescence (TRPL) dynamics (Figure S11),

we also determined the monomolecular trap-assisted recombination constants and the

bimolecular free electron-hole recombination constants for these $CsSnI_3$ films (Table S1).

Compared to the leaded $CH_3NH_3PbI_3$ perovskites with typical monomolecular recombination

coefficients of ~10 μs^{-1}, the 20% SnF_2-treated $CsSnI_3$ yields a coefficient of ~720 ($\pm$200) μs^{-1}

(*i.e.*, ~2 orders higher) – indicating much higher trap densities. However, the bimolecular

recombination constant of the 20% SnF_2-treated $CsSnI_3$ is ~10^{-8} $cm^3 s^{-1}$, which is 1-2 orders

larger than their leaded $CH_3NH_3PbI_3$ counterparts (9.4×10^{-10} - 8.7×10^{-11} $cm^3 s^{-1}$).[18] The origin

of large bimolecular recombination rate associated with Sn-based perovskites is still unclear

at this stage and further investigations are warranted.[35] Despite the higher trap concentrations, an acceptable density of traps could still be effectively filled with the use of higher pump excitations. Essentially, the larger bimolecular recombination constant for the 20% SnF_2-treated $CsSnI_3$ would play a vital role for its superior gain properties that is comparable to $CH_3NH_3PbI_3$. These results clearly suggest that such lead-free $CsSnI_3$ perovskite are more suited for light emitting applications rather than for light harvesting.

It is clear that SnF_2 addition has a profound effect on the optical gain. Previously, from thermodynamic analysis, the Sn vacancy formation energy was predicted to increase with SnF_2 addition.[33] The trap densities in the treated $CsSnI_3$ film are therefore expected to be reduced. This was accompanied by a reduction in the carrier densities in the $CsSnI_3$ film, however no direct evidence of trap reduction was presented. Transient absorption (TA) spectroscopy which allows us to monitor the state-filling of the traps was thus performed. Following photoexcitation with above bandgap 650 nm pump pulses, the hot charge carriers rapidly relax to the band edge (Figure S12). **Figure 3**a shows the pseudo color plots of the change in absorption (ΔA represented by the color scale) against wavelength (nm) and probe time delay (ps) for the four samples. With increasing SnF_2 addition, Figure 3a shows a prominent valley-like feature emerging near the bandgap at around 950 nm. Figure 3b gives the overlaid TA spectra of the four samples extracted from Figure 3a at 5 ps probe time delay. The untreated film (Figure 3a & 3b - black trace) yields a broad featureless negative ΔA band or photobleaching (PB) signature at wavelengths >950 nm, but a positive ΔA band or photoinduced absorption (PIA) signature at wavelengths <950 nm. In contrast, the SnF_2-added $CsSnI_3$ films (Figure 3b – red (5%), olive (10%) and blue (20%)) shows a PB signature with the PB valley at around 950 nm becomes progressively stronger. A PB signature could possibly arise from: (i) near bandgap stimulated emission of the carriers; and/or (ii) state-filling of the band edge states; or (iii) state-filling of the trap states. Mechanisms (i) and (ii) would account for the 950 nm PB valley near the bandgap in the SnF_2-added $CsSnI_3$ films –

7

which we term as PB1 in Figure 3b & 3c. On the other hand, the nearly-flat and broad PB band observed for the untreated $CsSnI_3$ films is consistent with mechanism (iii) – as shown in the schematic in Figure 3c as PB2. This suggests a prevalence of trap states, possibly from Sn vacancies functioning as intrinsic defects.[27-33] Indeed, the amplitude ratio of PB2 to PB1 is greatly reduced in the treated $CsSnI_3$ film (Figure 3b) – consistent with a reduction in the relative trap density. TA measurements thus provide a clear direct evidence for the trap state reduction. Furthermore, using the pump fluence dependent $I_{PL}[t = 0]$ approach described earlier, the density of the unintentionally-doped charge carriers for the 5%, 10% and 20% SnF_2 added $CsSnI_3$ films are estimated to be: $\sim 1.5 \times 10^{17}/cm^3$, $\sim 7.6 \times 10^{16}/cm^3$ and $\sim 2.8 \times 10^{16}/cm^3$, respectively (Figure 2b & S17). However, for the untreated $CsSnI_3$, the absence of any linear to quadratic transition in the investigated pump fluence range indicates that its doped charge carrier concentration is larger than $5.7 \times 10^{17}/cm^3$, consistent with Hall measurements.[33] Further characterization of this SnF_2-treated $CsSnI_3$ films with multi-techniques (XRD, EDS, SEM, PL) suggests that doping the precursor solution with SnF_2 of proper concentration could help $CsSnI_3$ better crystallized in orthorhombic phase with large crystal size and film coverage. However, I^- in the perovskite crystal are not partially substituted by the F^-. The SnF_2 is most likely localized at the surface and boundaries of $CsSnI_3$ crystals (See Supporting information for details).

Akin to their leaded counterparts, these $CsSnI_3$ thin films also exhibit excellent photo-stability under sustained optical pumping at 1 KHz repetition rate at room temperature (**Figure 4**a). The near invariance of the output ASE intensity with a standard deviation of 7 % about the mean intensity even for the lowest 5% added films under ~20 hours continuous irradiation (*i.e.*, $\sim 10^8$ laser shots in all) bears testimony to the excellent optical stability of these lead-free perovskite gain media (with equivalent stability for 20% SnF_2-treated samples – Figure S21). Such stability is superior to the state-of-the-art organic semiconducting thin films (50% drop in output power after $\sim 10^7$ laser shots)[10] and colloidal QDs (50% drop in output power after

~10^6 laser shots)[11]. Lastly, one of the greatest advantages of these low-temperature solution-processable halide perovskite gain media is their facile wavelength tunability using straight-forward mixing of their precursors. Figure 4b shows that the ASE peak could be tuned at room temperature from 700 nm to 950 nm by varying the bromides and iodides composition to obtain $CsSnBr_3$, $CsSnBr_2I$, $CsSnBrI_2$ and $CsSnI_3$ thin films. With 500 nm pumping (50fs, 1KHz), their ASE thresholds were determined to be 19 ± 4, 25 ± 5, 12 ± 2, 8 ± 2 $\mu J/cm^2$, respectively. The trend of the bandgap variation with composition is qualitatively consistent with theoretical predictions based on the Δ-sol method, as shown in Figure S22. Unlike leaded halide perovskites (e.g. $CH_3NH_3PbCl_xBr_{3-x}$ or $CH_3NH_3PbBr_yI_{3-y}$)[22-24] which are limited to around 800 nm, the gain bandwidth of these Pb-free $CsSnX_3$ (X = Br and I) perovskites is now extended to above 1μm (Figure S10), the spectrally important NIR spectroscopy regime for in vivo imaging at the transparent windows,[36] pharmaceutical and manufacturing quality control.[37] Importantly, our findings point to a straight-forward strategy of facile cationic and halide replacement in unleaded perovskites to access the NIR regime that has so far been rather elusive with traditional solution-processable gain media like organics and inorganic colloidal quantum dots. With high quality single crystal nanowires or nanoplatelets of the SnF_2 treated $CsSnI_3$, the coherent light emission threshold could be further greatly reduced.[23] Such single crystals may hold the key to realizing electrically-driven lasers.

In summary, Sn-based perovskites are demonstrated as a new model perovskite system for light emission applications. SnF_2-addition effectively suppresses the trap states in solution-processed Sn-based perovskites and the coherent light emission originates from the free electron-hole bimolecular recombination with a high rate of ~10^{-8} cm^3s^{-1} (*i.e.*, ~1-2 orders larger than $CH_3NH_3PbI_3$). Therefore, the lead-free Sn-based halide perovskite, despite exhibiting very poor photovoltaic performance, possesses exceptional optical gain properties in the NIR up to ~1 μm. The light emission properties of these Sn-based perovskites are

comparable or even better than the lead-based perovskites. The solution-processability of these Sn-based perovskites gain media would find niche applications that require non-conformal, non-planar geometries on flexible substrates. This has tremendous implications for the area of light emitting diodes, since it indicates that lead free perovskites with much poorer electronic properties would still be able to form efficient light emitters.

Experimental Details

The inorganic lead-free perovskite ($CsSnI_3$) films were prepared by a low-temperature solution method. Stoichiometric mixed CsI (Sigma-Aldrich, 99.9%) and SnI_2 (Sigma-Aldrich, 99.99%) powder with appropriate amount of SnF_2 was dissolved in polar organic solvents (dimethy1 sulfoxide (DMSO)) to give transparent yellow solutions (0.6 M) under nitrogen environment at room temperature. Black thin films are obtained by spincoating the solution (80 µL) on quartz substrates (2 cm × 2 cm) with subsequent annealing at 100 ℃ for 30 minutes. Poly (methyl methacrylate) (PMMA, 15 mg/mL in Chlorobenzene) was coated on the $CsSnI_3$ films to avoid degradation of the perovskites during optical measurements.

The butterfly wings are soaked in ethanol at room temperature for 6 hours to remove impurities on the wings. At the end of 6 hours, the wings are carefully retrieved and rinsed again with ethanol. The excess solvent is subsequently removed by placing the wings in a vacuum chamber for drying. The dried wings are then stored under vacuum prior to perovskite dropcasting.

For femtosecond optical spectroscopy, the laser source was a Coherent Libra™ regenerative amplifier (50 fs, 1 KHz, 800 nm) seeded by a Coherent Vitesse™ oscillator (50 fs, 80 MHz). 800 nm laser pulses were from the regenerative amplifier. 650-nm laser pulses were generated from a Coherent OPerA-Solo optical parametric amplifier. The laser pulses (of spot size ~1.5 mm in diameter) were directed to the samples in an optical cryostat under vacuum. The emission from the samples was collected at a backscattering angle of 150° by a pair of lenses

and into an optical fiber that is coupled to a spectrometer (Acton, Spectra Pro 2300i) with an InGaAs array photodetector (PyLoN-IR:1024). TRPL was collected using an Optronis Optoscope[TM] streak camera system which has an ultimate temporal resolution of ~10 ps. Broad band femtosecond transient absorption spectra of the perovskite films were taken using the Ultrafast System HELIOS[TM] transient absorption spectrometer. The broadband NIR probe pulses (800-1600 nm) were generated by focusing a small portion (~10 μJ) of the fundamental 800 nm laser pulses into a 10 mm thick sapphire plate. Room temperature photoluminescence quantum yield (PLQY) of the lead-free perovskite thin films were measured using an integrating sphere. The samples were excited with 650 nm pulses generated from the Coherent OPerA-Solo. The emission was corrected for CCD and grating responsivity. Room temperature gain measurements were carried out using a standard VSL method. The excitation stripe was focused by a cylindrical lens (with focal length f = 20 cm) to a stripe (of dimensions ~ 5 mm × 0.5 mm) and the emission collection configuration was the same as described above. The excitation stripe length was varied through an adjustable slit actuated by a micrometer which was placed at the focal line of the cylindrical lens.

Received: ((will be filled in by the editorial staff))
Revised: ((will be filled in by the editorial staff))
Published online: ((will be filled in by the editorial staff))

_[1]   R. N. Hall, G. E. Fenner, J. D. Kingsley, T. J. Soltys, R. O. Carlson, *Phys. Rev. Lett*. **1962**, *9*, 366.

_[2]   W. W. Chow, S. W. Koch, *Semiconductor-Laser Fundamentals*, Springer, Berlin, **1999**.

_[3]   X. Duan, Y. Huang, R. Agarwal, C. M. Lieber, *Nature* **2003**, *421*, 241.

_[4]   J. Yoon, S. Jo, I. S. Chun, I. Jung, H. S. Kim, M. Meitl, E. Menard, X. Li, J. J. Coleman, U. Paik, J. A. Rogers, *Nature* **2010**, *465,* 329.

_[5]   R. Chen, T. T. D. Tran, K. W. Ng, W. S. Ko, L. C. Chuang, F. G. Sedgwick, C. C. Hasnain, *Nature Photon.* **2011**, *5*, 170.

_[6]   K. Tanabe, K. Watanabe, Y. Arakawa, *Sci. Rep.* **2012**, *2*, art. no 349.

_[7]   V. G. Kozlov, V. Bulovic, P. E. Burrows, S. R. Forrest, *Nature*, **1997**, *389*, 362.

_[8]   E. B. Namdas, M. Tong, P. Ledochowitsch, S. R. Mednick, J. D. Yuen, D. Moses, A. J. Heeger, *Adv. Mater.* **2009**, *21*, 799.

_[9]   J. Clark, G. Lanzani, *Nature Photon.* **2010**, *4*, 438.

_[10]   C. Grivas, M. Pollnau, *Laser Photon. Rev*. **2012**, *6*, 419.

_[11]   P. T. Snee, Y. Chan, D. G. Nocera, M. G. Bawendi, *Adv. Mater.* **2005**, *17*, 1131.

_[12]   V. I. Klimov, *Annu. Rev. Phys. Chem.* **2007**, 58, 635.

_[13]   C. Dang, J. Lee, C. Breen, J. S. Steckel, S. C. Sullivan, A. Nurmikko, *Nat. Nanotechnol.* **2012**, *7*, 335.

_[14]   G. Agrawal, N. Dutta, Recombination Mechanisms in Semiconductors, in Semiconductor Lasers, Springer, US. **1993**, p. 74-146.

_[15]   A. Kojima, K. Teshima, Y. Shirai, T. Miyasaka, *J. Am. Chem. Soc.* **2009**, *131*, 6050.

_[16]   H. S. Kim, C. R. Lee, J. H. Im, K. B. Lee, T. Moehl, A. Marchioro, S. J. Moon, R. H. Baker, J. H. Yum, J. E. Moser, M. Grätzel, N. G. Park, *Sci. Rep.* **2012**, *2*: 591.

_[17]   M. M. Lee, J. Teuscher, T. Miyasaka, T. N. Murakami, H. J. Snaith, *Science* **2012**, *338*, 643.

_[18]   C. Wehrenfennig, G. E. Eperon, M. B. Johnston, H. J. Snaith, L. M. Herz, *Adv. Mater*. **2014**, *26*, 1584.

_[19]   G. Xing, N. Mathews, S. Sun, S. S. Lim, Y. M. Lam, M. Grätzel, S. Mhaisalkar, T. C. Sum, *Science* **2013**, *342*, 344.

_[20]   S. D. Stranks, G. E. Eperon, G. Grancini, C. Menelaou, M. J. P. Alcocer, T. Leijtens, L. M. Herz, A. Petrozza, H. J. Snaith, *Science* **2013**, *342*, 341.

_[21]   N. J. Jeon, J. H. Noh, W. S. Yang, Y. C. Kim, S. Ryu, J. Seo, S. II. Seok, *Nature* **2015**, *517*, 476.

_[22]   G. Xing, N. Mathews, S. S. Lim, N. Yantara, X. Liu, D. Sabba, M. Grätzel, S. Mhaisalkar, T. C. Sum, *Nat. Mater.* **2014**, *13*, 476.

_[23]   a) H. Zhu, Y. Fu, F. Meng, X. Wu, Z. Gong, Q. Ding, M. V. Gustafsson, M. T. Trinh, S. Jin, X. Y. Zhu, *Nat. Mater.* **2015**, *14*, 636; b) Q. Zhang, S. T. Ha, X. Liu, T. C. Sum, Q. Xiong, *Nano Lett*. **2014**, *14*, 5995; c) S. W. Eaton, M. Lai, N. A. Gibson, A. B. Wong, L. Dou, J. Ma, L. Wang, S. R. Leone, P. Yang, *Proc. Natl. Acad. Sci*. **2016**, *113*, 1993; d) W. Zhang, L. Peng, J. Liu, A. Tang, J. Hu, J. Yao, Y. S. Zhao, *Adv. Mater*. **2016**, DOI: 10.1002/adma.201505927; e) M. Saliba, S. M. Wood, J. B. Patel, P. K. Nayak, J. Huang, J. A. Alexander-Webber, B. Wenger, S. D. Stranks, M. T. Horantner, J. T. Wang, R. J. Nicholas, L. M. Herz, M. B. Johnston, S. M. Morris, H. J. Snaith, M. K. Riede, *Adv. Mater*. **2015**, *28*, 923; f) S. Chen, K. Roh, J. Lee, W. K. Chong, Y. Lu, N. Mathews, T. C. Sum, A. Nurmikko, *ACS Nano* **2016**, *10*, 3959;

_[24]   S. Yakunin, L. Protesescu, F. Krieg, M. I. Bodnarchuk, G. Nedelcu, M. Humer, G. D. Luca, M. Fiebig, W. Heiss, M. V. Kovalenko, *Nat. Commun.* **2015**, *6*, 8056.

_[25] Z. K. Tan, R. S. Moghaddam, M. L. Lai, P. Docampo, R. Higler, F. Deschler, M. Price, A. Sadhanala, L. M. Pazos, D. Credgington, F. Hanusch, T. Bein, H. J. Snaith, R. H. Friend, *Nat. Nanotechnol.* **2014**, *9*, 687.

_[26]   H. Cho, S. H. Jeong, M. H. Park, Y. H. Kim, C. Wolf. C. L. Lee, J. H. Heo, A. Sadhanala, N. Myoung, S. Yoo, S. H. Im, R. H. Friend, T. W. Lee, *Science* **2015**, *350*, 1222.

_[27] K. Shum, Z. Chen, J. Qureshi, C. Yu, J. J. Wang, W. Pfnninger, N. Vockic, J. Midgley, J. T. Kenney, *Appl. Phys. Lett.* **2010**, *96*, 221903.

_[28] I. Chung, B. Lee, J. He, R. P. H. Chang, M. G. Kanatzidis, *Nature* **2012**, *485*, 486.

_[29] I. Chung, J. H. Song, J. Im, J. Androulakis, C. D. Malliakas, H. Li, A. J. Freeman, J. T. Kenney, M. G. Kanatzidis, *J. Am. Chem. Soc.* **2012**, *134*, 8579.

_[30] L. Huang, W. R. L. Lambecht, *Phys. Rev. B* **2013**, *88*, 165203.

_[31] F. Hao, C. C. Stoumpos, D. H. Cao, R. P. H. Chang, M. G. Kanatzidis, *Nature Photon.* **2014**, *8*, 489.

_[32] N. K. Noel, S. D. Stranks, A. Abate, C. Wehrenfennig, S. Guarnera, A. A. Haghighirad, A. Sadhanala, G. E. Eperon, S. K. Pathak, M. B. Johnston, A. Petrozza, L. M. Herz, H. J. Snaith, *Energy Environ. Sci.* **2014**, *7*, 3061.

_[33] M. H. Kumar, S. Dharani, W. L. Leong, P. P. Boix, R. R. Prabhakar, T. Baikie, C. Shi, H. Ding, R. Ramesh, M. Asta, M. Grätzel, S. G. Mhaisalkar, N. Mathews, *Adv. Mater.* **2014**, *26*, 7122.

_[34] M. Saba, M. Cadelano, D. Marongiu, F. Chen, V. Sarritzu, N. Sestu, C. Figus, M. Aresti, R. Piras, A. G. Lehmann, C. Cannas, A. Musinu, F. Quochi, A. Mura, G. Bongiovanni, *Nat. Commun.* **2014**, *5*, 5049.

_[35] C. Motta, F. EI-Mellouhi, S. Kais, N. Tabet, F. Alharbi, S. Sanvito, *Nat. Commun.* **2015**, *6*, 7026.

_[36] A. M. Smith, M. C. Mancini, S. Nie, *Nat. Nanotechnol.* **2009**, 4, 710-711.

_[37] R. C. Lyon, D. S. Lester, E. N. Lewis, E. Lee, L. X. Yu, E. H. Jefferson, A. S. Hussain, *et al. AAPS PharmSciTech.* **2002**, *3*, 17.
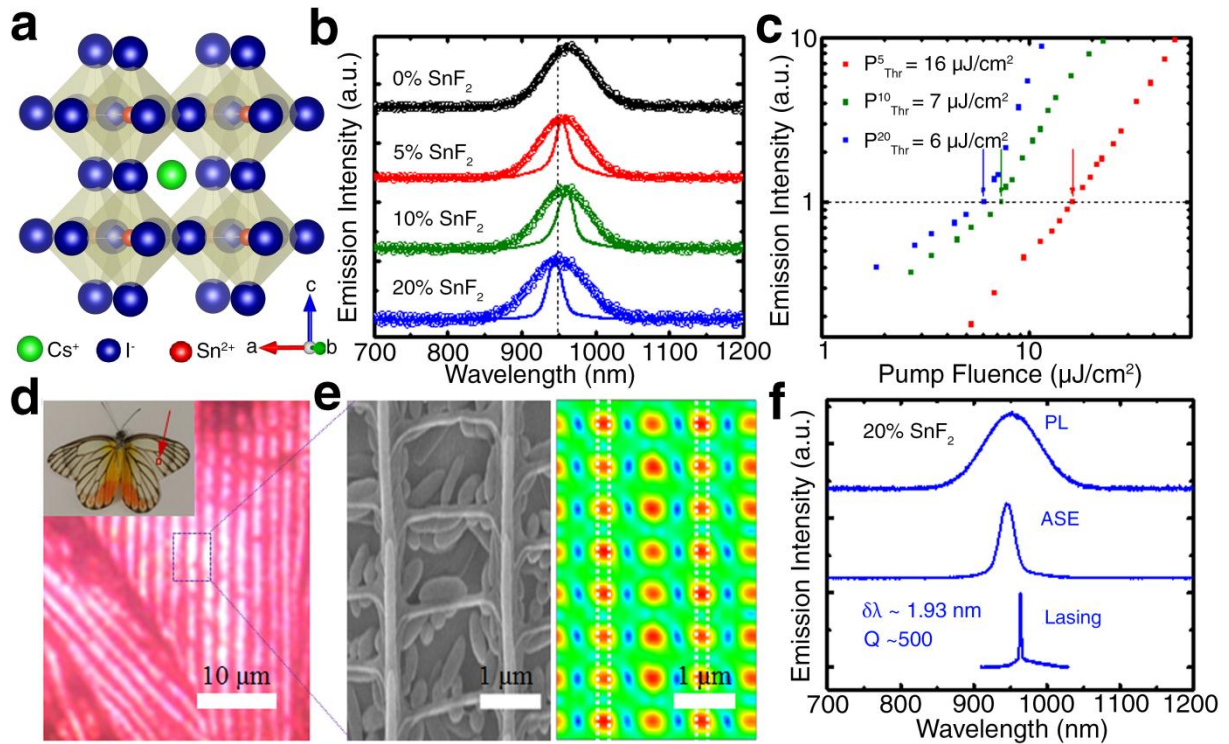
Figure 1. ASE and Lasing from lead-free perovskite. **a**) Typical ABX$_3$ perovskite structure. **b**) Normalized emission at low pump fluence (open circles, ~1 μJ/cm^2) and high pump fluence (solid lines, ~70 μJ/cm^2) for CsSnI$_3$ with different molar concentrations of SnF$_2$ treatment. **c**) Variable fluence measurements reveal the ASE thresholds of the SnF$_2$-treated samples. **d**) Optical micrograph of a butterfly scale from the white part of the wing. Inset is a photograph of the butterfly (genus: *delias hyparete metarete*). **e**) SEM image showing lamellae (vertical structures) in the scale. Simulated electric field distribution at resonant cavity mode (950 nm) with embedded CsSnI$_3$. The white dotted lines indicate the approximate locations of the lamella. **f**) A comparison of the PL, ASE and single mode lasing of CsSnI$_3$ (20% SnF$_2$). These optical experiments were performed using 650 nm wavelength pump pulses (50fs, 1KHz).
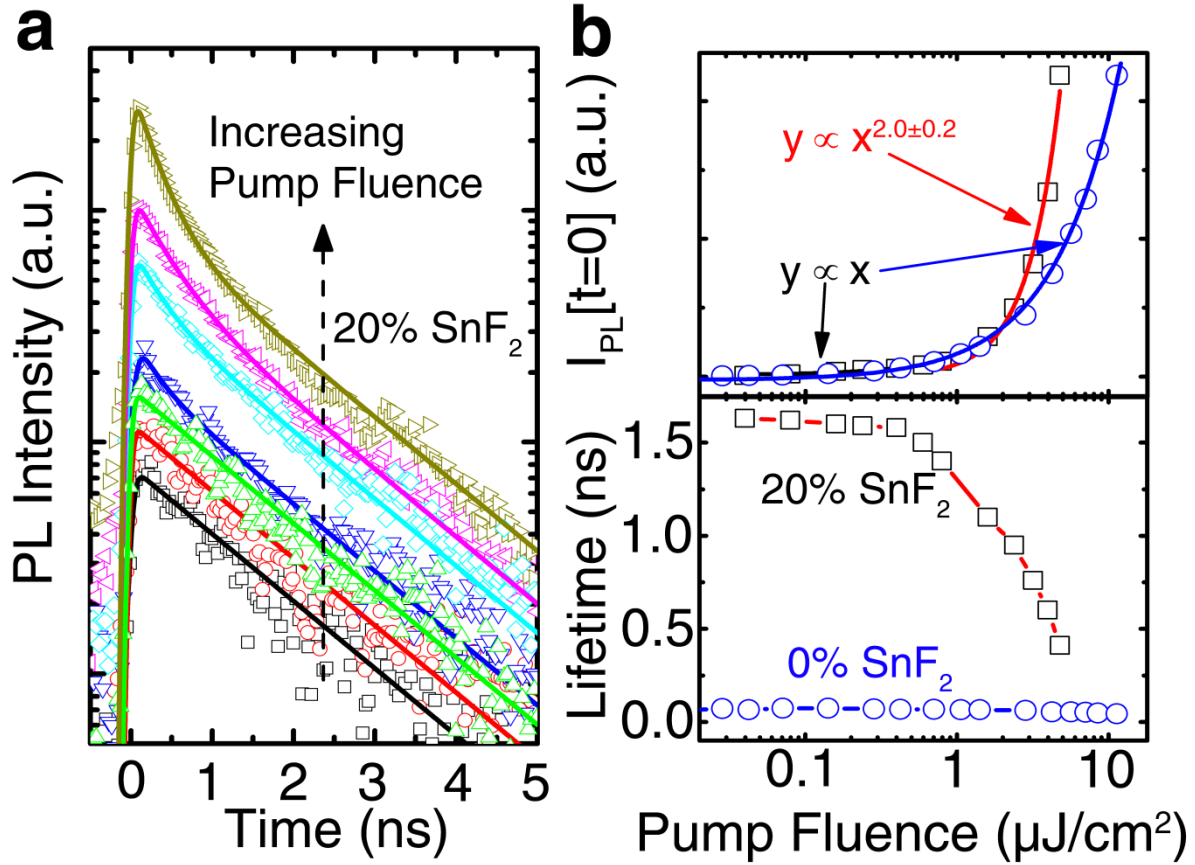
Figure 2. Free electron-hole recombination in CsSnI$_3$ from Transient PL spectroscopy. **a**) PL decay transients of 20% SnF$_2$-added CsSnI$_3$ film with varying pump fluence (where only selected decays at the pump fluence of 0.2, 0.4, 0.6, 0.8, 1.6, 2.4 and 4.0 µJ/cm^2 are presented). **b**) Pump fluence dependence of the initial time PL intensity, $I_{PL}(0)$ (upper panel) and the effective PL lifetime (lower panel) for the 0% (blue circle) and 20% (black square) SnF$_2$-added films. The data of 20% SnF$_2$-added film shows a trap-assisted recombination (linear dependence) and a free-carrier bimolecular recombination (quadratic dependence) at low and higher pump fluence, respectively. The absence of any linear to quadratic transition for the pristine CsSnI$_3$ film indicates that its trap density is much higher than the photo-injected charge carrier concentration. The optical excitation was performed with 650 nm pump pulses (50fs, 1KHz).

16
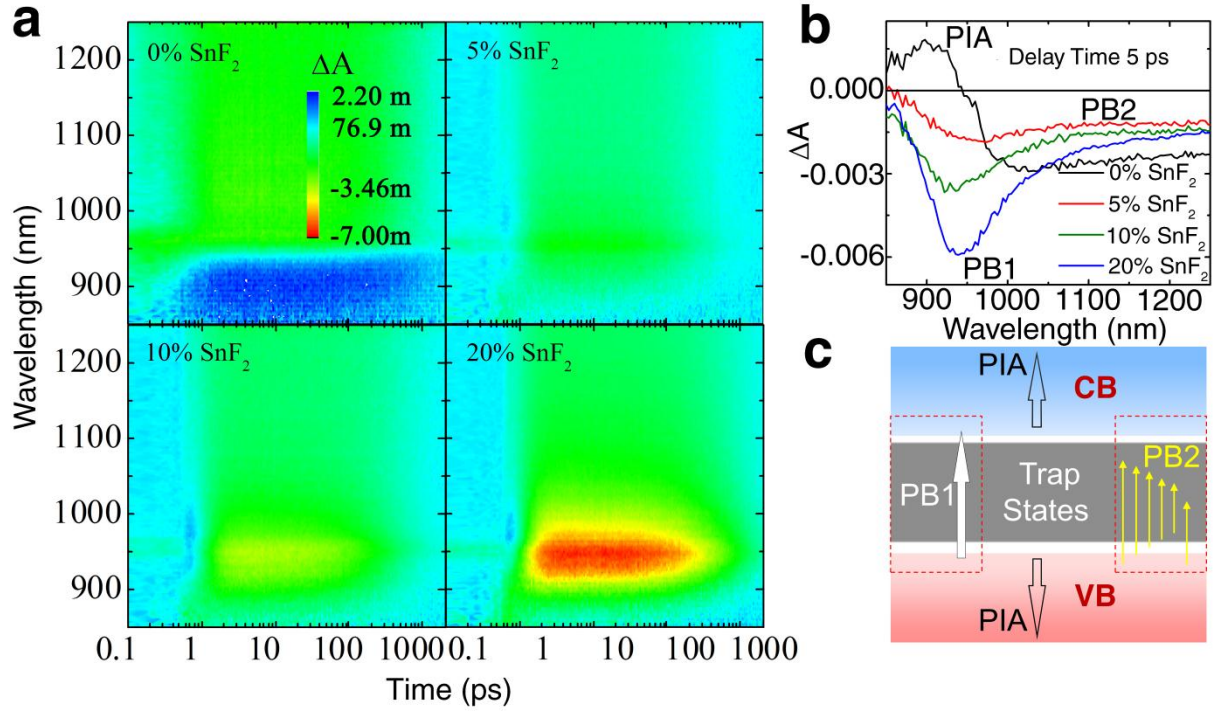
Figure 3. TA Spectroscopy and Data Interpretation. **a**) Pseudo color TA plot showing the change in absorption (ΔA) as a function of probe wavelength and probe delay time for the CsSnI$_3$ samples with different SnF$_2$ treatment. Note the absence of the band edge PB valley (950 nm) in untreated film, where this feature gradually becoming more prominent with increasing SnF$_2$ addition. The experiments were conducted with 650 nm pump pulses (50fs, 1KHz) at a pump fluence of ~2 μJ/cm^2. **b**) TA spectra of the four samples at 5 ps probe delay time (extracted from the TA plots in (a)) are overlaid for comparison. **c**) A schematic diagram illustrating the origins of the various TA features of PB and PIA.
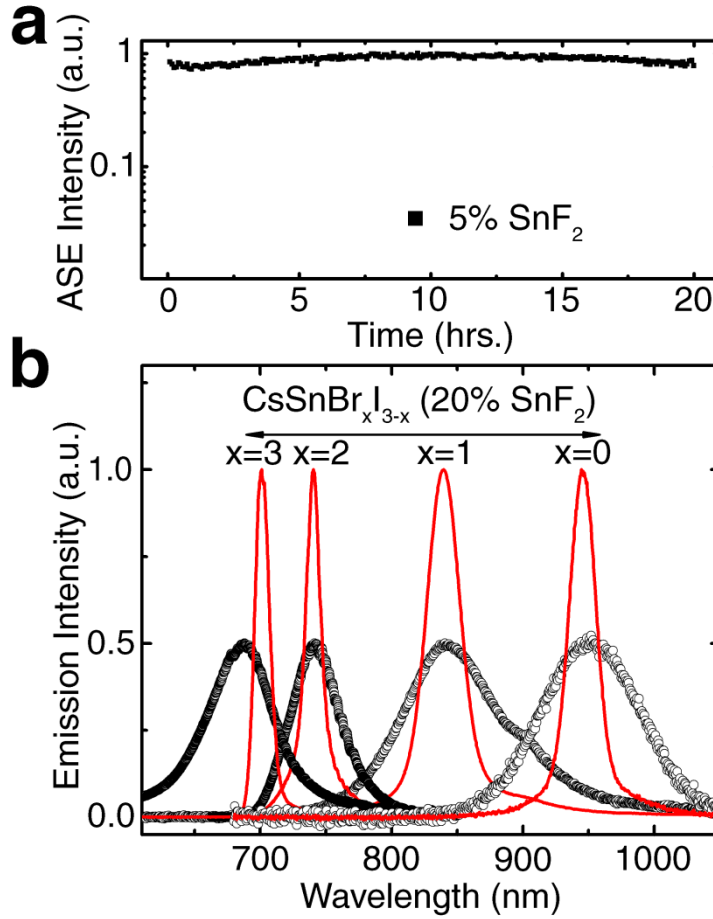
Figure 4. Robust & Tunable NIR PL and ASE from CsSnBr$_x$I$_{3-x}$ mixed perovskites. **a**) Time-dependent ASE intensity of the 5% SnF$_2$-treated CsSnI$_3$ film with a pump fluence of 70 µJ/cm^2 (600 nm, 50 fs, 1KHz) under excitation for ~20 hours performed at room temperature. High stability is evident even for the lowest SnF$_2$ addition. **b**) Wide PL and ASE wavelength tunability from CsSnBr$_x$I$_{3-x}$ films fabricated by facile mixing the precursor solutions. The experiments were conducted with 500 nm pump pulses (50fs, 1KHz).

The table of contents entry: **The family of solution-processed tin-based perovskites is demonstrated as a new and superior near infrared gain medium**. Due to the large electron-hole bimolecular recombination associated with tin and reduced trap density with SnF_2 treatment, these lead-free "green" perovskites yield stable coherent light emission extending to ~1µm at strikingly low thresholds.

G. Xing, M. H. Kumar, W. K. Chong, X. Liu, Y. Cai, H. Ding, M. Asta, M. Grätzel, S. Mhaisalkar, N. Mathews*, and T. C. Sum*

Title: Solution-Processed Tin-Based Perovskite for Near Infrared Lasing

ToC figure
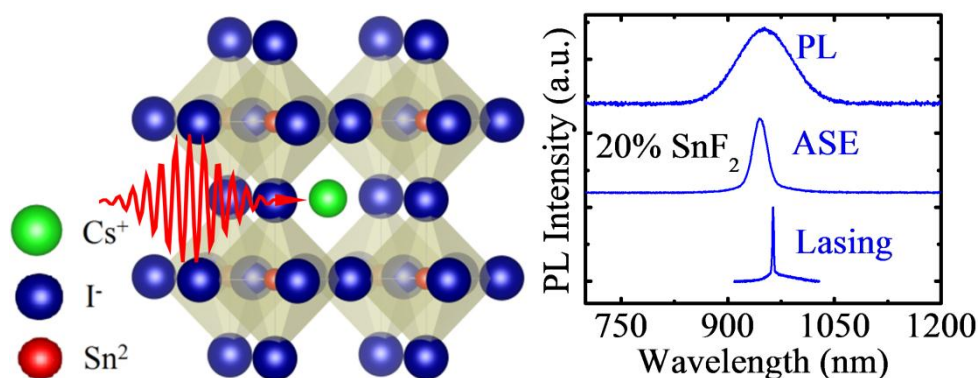
Supporting Information:

Solution-Processed Tin-Based Perovskite for Near Infrared Lasing

By Guichuan Xing, Mulmudi Hemant Kumar, Wee Kiang Chong , Xinfeng Liu, Yao Cai, Hong Ding, Mark Asta, Michael Grätzel, Subodh Mhaisalkar, Nripan Mathews*, and Tze Chien Sum*

((Optional Dedication))

[*]   Dr.   G.   Xing,   W.   K.   Chong,   Dr.   X.   Liu,   Prof.   T.   C.   Sum
Division of Physics and Applied Physics, School of Physical and Mathematical Sciences
Nanyang   Technological   University,   21   Nanyang   Link,   637371   (Singapore)
E-mail: Tzechien@ntu.edu.sg
        Dr. M. H. Kumar, Prof. S. Mhaisalkar, Prof. N. Mathews
Energy Research Institute @NTU (ERI@N), Research Techno Plaza, X-Frontier Block, Level 5, 50 Nanyang Drive, 637553 (Singapore)
School of Materials Science and Engineering, Nanyang Technological University, Nanyang Avenue, 639798 (Singapore)
E-mail: Nripan@ntu.edu.sg
        Y. Cai, Dr. H. Ding, Prof. M. Asta
Department of Materials Science and Engineering, University of California, Berkeley, CA 94720 (USA)
        Prof. M. Grätzel
Energy Research Institute @NTU (ERI@N), Research Techno Plaza, X-Frontier Block, Level 5, 50 Nanyang Drive, 637553 (Singapore)
Laboratory of Photonics and Interfaces, Department of Chemistry and Chemical Engineering, Swiss Federal Institute of Technology, Station 6, CH-1015 Lausanne, Switzerland.
        Dr. G. Xing
Present address: Key Laboratory of Flexible Electronics (KLOFE) & Institute of Advanced Materials (IAM), Jiangsu National Synergetic Innovation Center for Advanced Materials (SICAM), Nanjing Tech University (Nanjing Tech), 30 South Puzhu Road, Nanjing 211816, China
        Dr. M. H. Kumar
Present address: Research School of Engineering, The Australian National University, Canberra, Australia 2601
        Dr. X. Liu
Present address: CAS Center for Excellence in Nanoscience & CAS Key Laboratory of Standardization and Measurement for Nanotechnology, National Center for Nanoscience and Technology, Beijing 100190, China

1. **Dominant factors limiting amplified spontaneous emission (ASE) and lasing from narrow gap inorganic and organic semiconductors**

The development of near infrared laser with low band gap semiconductors typically is limited by the low quantum efficiency (QE) of the gain materials and magnified Auger losses with decreasing bandgap.[1-14] Auger recombination is a type of non-radiative process that becomes significant for high injected carrier densities (N) in semiconductors. In an inorganic semiconductor, the Auger process involves a three-particle interaction where the energy and momentum from the recombination of an electron and hole are transferred to a third particle (electron or hole). This nonradiative process at high carrier densities is undesirable for ASE as it impedes gain buildup and increases the ASE threshold. The Auger process in semiconductors can be quantified by Auger recombination rate (R_a) or its auger coefficient (C) where it can be expressed as follows:

$$R_a = CN^3 \tag{S1}$$

The Auger coefficient varies among bulk semiconductors and is highly dependent on several intrinsic properties, such as bandgap and temperature. Its dependence on bandgap (E_g) can be derived using Fermi's golden rule, Bloch functions and a series of approximations.[14,38] The resulting expression of R_a provides more insights and can be expressed as:

$$R_a \propto n^2 p e^{-\frac{BE_g}{K_B T}} \tag{S2}$$

Where k_B is the Boltzmann constant, T is the temperature, n and p are the electron and hole concentration respectively and B is a constant. The exponential relation shown in Eq. S2 suggests that Auger recombination is more severe for small band gap semiconductor and can be challenging to realize near-infrared (NIR) ASE or lasing. In quantum confined systems (e.g., quantum dot, quantum well, quantum wires etc), the spatial confinement of the photo-generated charge carriers will drastically increase the Auger rates.[12,14]

In the case of organic semiconductors with typical Frenkel excitons of large exciton binding energy, the dominant non-radiative process affecting ASE and lasing is the exciton-exciton annihilation process, which is also particularly strong in small bandgap organic semiconductors. Further stumbling blocks include intrinsic losses from fast nonradiative decay as well as the conflicting requirements of high charge carrier mobility (which require overlap of π-electron systems) and large stimulated emission (which require the chromophores to be well separated).[7-10]

2. **Crystallizations of CsSnI₃ films treated with SnF₂ in precursor solution**

The X-ray diffraction (XRD) patterns of the films (Figure S1) indicate that perovskites are crystallized in the orthorhombic (Pnam) structure.[27-33] With additional SnF₂ in the precursor solution, no obvious change in lattice parameters and crystalline phase is observed. However, the two weak peaks originated from non-orthorhombic perovskite phase in the pure CsSnI₃ film are totally eliminated with the SnF₂ doping. This clearly shows that the samples are better crystallized in the orthorhombic phase with SnF₂ treatment. The result also suggests that I⁻ in the perovskite crystal are not partially substituted by F⁻. Otherwise, the lattice parameters will be changed.

Secondly, based on the PL measured and presented in Figure 1b, no significant emission peak shifting has been observed from the perovskite films prepared with additional SnF₂ doping in the precursor solution, which also suggests that the I⁻ in the perovskite crystal are not partially substituted by the F⁻. This kind of partial substitution is not preferred here due to the large ionic radii difference between I (2.20 Å) and F (1.33 Å). The slight emission peak shift, with peak values of 964 nm, 957 nm, 959 nm and 952 nm for the 0%, 5%, 10% and 20% SnF₂-added CsSnI₃ films respectively, could be induced by changes to the dielectric

environment, film morphology and bandgap tail states caused by the SnF_2 treatment. However, the SnF_2 doping in the precursor solution can effectively passivate the surface dangling bonds and possibly some inside I^- vacancies of the $CsSnI_3$ perovskite crystal and reduce the middle gap trap states, which are clearly evidenced from the transient absorption (TA) spectra (Figure 3 and main text, paragraph 7).

EDS mapping show that the Cs, Sn and I almost homogeneously distributed in the crystal (Figure S2). F is also distributed over the whole crystal, but is slightly more localized at the boundaries. Previous XPS measurements had shown that the F is uniformly distributed through the thickness of the $CsSnI_3$ film Together with the previous XRD and PL results, we suggest that the SnF_2 is most likely localized at the surface and boundaries of $CsSnI_3$ crystals. This conclusion is also consistent with previous XPS observation that the F^- remained in the final films without chemical bonding to $CsSnI_3$.[33]

The SEM images clearly show that SnF_2-treatment improves the crystallization quality (Figure S3). For the pristine film, the $CsSnI_3$ only crystallized into small size crystals (~1 μm). These small crystals would give rise to large scattering (optical loss) and higher concentration surface states, which would be detrimental to the optical gain buildup in the film. The crystal size increases with increasing the SnF_2 concentration with the best film morphology (*i.e.*, largest crystals and least number of pinholes) being achieved from precursor solution with additional 20% SnF_2.

3. ASE characterization

The pump fluence dependent photoluminescence (PL) and time-resolved PL (TRPL) clearly show a transition from spontaneous emission (SE) to ASE for the SnF_2-treated $CsSnI_3$ films for increasing pump fluence (Figure S4a). Below the threshold fluence (F_{Thr}), SE linearly increases with increasing pump fluence and dominates the light output from the films with a FWHM of ~80 nm. Above F_{Thr}, the emission bandwidth reduces to less than 25 nm and the emission intensity increases superlinearly with increasing the pump fluence (Figure 1c). These are clear signatures of optical gain from SnF_2-treated $CsSnI_3$ films. However, SE merely increases continually with increasing pump fluence in the untreated $CsSnI_3$ film, without ever achieving population inversion within the limits of its damage threshold (~ 200 μJ/cm^2).

As discussed in the earlier paragraphs of the supporting information, apart from trap states affecting the gain properties, fast nonradiative recombination from multi-particle effects (*e.g.*, bimolecular recombination and the 3 particle Auger processes) also present a major challenge for narrow bandgap materials. Remarkably, we find that the ASE in these SnF_2-treated $CsSnI_3$ perovskites can effectively compete with the multi-particle processes. Figure S4b shows the PL decay transients of the transition from SE to ASE for the 20% SnF_2-treated $CsSnI_3$ film. At a pump fluence just below the ASE threshold (~5 μJ/cm^2), the charge carrier radiative recombination decay dynamics exhibit a short lifetime component of ~110 ± 5 ps that is dominated by multi-particle recombination (including free electron-hole bimolecular recombination). For comparison at very low pump fluence (~1 μJ/cm^2), the trap-state assisted single exponential lifetime is 1.6 ± 0.1 ns (Figure 2b). Above the ASE threshold fluence (~ 8 μJ/cm^2), a very prominent ultrashort lifetime component of <10 ps appears in addition to the multi-particle dominated decay lifetime (83 ± 2 ps). This ultrashort lifetime component is attributed to the ASE where the measured 10 ps lifetime is in fact due to the limitations of the streak camera's system temporal response.

Figures S5a-c show the representative emission spectra near the ASE threshold. Figure S5d-f show the detailed emission intensity and emission FWHM *vs* pump fluence. The conventional way of determining the threshold is through examining the curvature of the intensity *vs*. power and the narrowing of the peak. Mathematically, it is the intersection of the

SE power dependent fit with the ASE power dependent fit. The extracted ASE thresholds for these samples clearly show that the ASE threshold decreases with increasing the SnF_2 treatment concentration in the precursor solution.

Figure S6a shows the pump-fluence dependent PL quantum yield (PLQY) of the 20% SnF_2-treated $CsSnI_3$ film measured with an integrating sphere. The samples were excited with 650 nm pulses generated from the optical parametric amplifier (Coherent OPerA-Solo). The emission was corrected for CCD and grating responsivity. At low pump fluence of ~4 $\mu J/cm^2$, the PLQY is found to be ~3.0 ± 0.5 %. Comparatively, the pristine and the 0%, 5%, and 10% SnF_2-treated $CsSnI_3$ films yielded PLQYs of 0.6 ± 0.1%, 1.1 ± 0.2% and 2.0 ± 0.3%, respectively. As expected, the PLQY increases with increased suppression of the trap states. With increasing pump fluence, the PLQY increases as the optical gain dominates the nonradiative recombination pathways. At pump fluence much larger than the ASE thresholds, a PLQY as large as 13 ± 1% is measured for the 20% SnF_2-treated $CsSnI_3$ film. This value is comparable to that measured for the leaded $CH_3NH_3PbI_3$ system under the same experimental conditions.[22]

With a relatively high PL quantum yield and inconsequential effects from the multiparticle recombination, large optical gain is therefore observed from these SnF_2-treated $CsSnI_3$ films. The room temperature net gains of the $CsSnI_3$ films were assessed using Variable Stripe Length (VSL) measurements (Figure S6b). The data is fitted using the method developed by Shaklee and Leheny,[39] which is a straightforward way to determine the net gain value of a material over the small signal regime (utilized for inorganic and organic semiconductors in slab geometry). The equation is:

$$I_0(z) = \frac{I_s A}{g}\left[\exp(gz) - 1\right] \tag{S3}$$

where $I_0(z)$, g, and z are the detected light intensity, gain coefficient and excitation stripe length, respectively; I_s is the SE rate per unit volume and A is the cross-sectional area of the excited volume.

With the above VSL method, net gains of 120 ± 10, 130 ± 10 and 200 ± 10 cm^{-1} are determined for the 5%, 10% and 20% SnF_2-treated $CsSnI_3$ films, respectively (Figure S6b). Comparatively, the gain of the 20% SnF_2-treated $CsSnI_3$ film is comparable with the leaded $CH_3NH_3PbI_3$ films[22] and $CsPbI_3$ nanocrystal films;[24] and is better than conjugated polymer thin films[7-10] and traditional colloidal nanocrystals[11-13].

4. Characterization & modeling the butterfly wing lasing

The typical SEM image shows that the 20% SnF_2-treated $CsSnI_3$ can infiltrate well into the butterfly wing (Figure S7). Under 650 nm laser pulse excitation with an optical microscope, single-mode threshold lasing from the $CsSnI_3$ (20% SnF_2) embedded in the butterfly wing (white part) was achieved as shown in Figure 1f & S8. A two-dimensional pseudo-colour plot of the emission spectra as function of pump fluence is shown in Figure S8a. Representative emission spectra which show the transition from SE to lasing are depicted in Figure S8b. Below lasing threshold, the SE shows a broad peak with a FWHM of ~ 76 nm. Above the lasing threshold, a sharp peak with a FWHM of ~ 1.93 develops rapidly with increasing the pump fluence. However, the broad SE intensity remains almost constant. The detail pump fluence dependent emission intensity and FWHM are shown in the inset of Figure S8b. The S-shape dependence of emission intensity on pump fluence and the rapid reduction of emission spectrum FWHM above certain pump fluence indicate single mode lasing operation here. The laser line exhibits a FWHM of ~1.9 nm (limited by the resolution of spectrometer) with a Q factor of ≥500 (the Q factor is calculated as $\lambda/\Delta\lambda$, where λ and $\Delta\lambda$ are the wavelength and the FWHM of the laser emission). This experimental result corresponds well with the cavity mode simulation (Figure 1e).

The cavity lasing modal and spectral simulation were performed using the three dimensional (3D) finite-difference time-domain (FDTD) simulation software (Lumerical[TM]) to understand the optical feedback mechanism that allows laser oscillation in the natural photonic crystal embedded with the 20% SnF$_2$-treated CsSnI$_3$ gain medium. Our simulations were performed with the following two steps: i) First determine the effective refractive index of the butterfly wing by comparing the measured micro-area and simulated reflection spectra (Figure S9) to determine the effective index (*i.e.*, $n_{eff} = 1.4$).; ii) Using n_{eff} determined in step 1, we then simulate the coherent light emission electromagnetic field distribution in the natural photonic cavity embedded with 20% SnF$_2$-treated CsSnI$_3$. The refractive index of CsSnI$_3$ is around 3.25 at 950nm ($n = 3.25$).[41] When lasing occurs in this perovskite-coated butterfly photonic crystal system, the parallel lamellas serve as the Fabry-Perot cavity and the electric field distributions at 950 nm are shown in Figure 1e.

Since the cavity mode is determined by gain material and butterfly parallel lamellas, the lasing mode should be tunable by changing the lamella interspacing. Figure S10 clearly shows that sharp lasing peak could be tuned in a large spectrum range by exciting the different position of the wing infiltrated with 20% SnF$_2$-treated CsSnI$_3$. Single mode lasing with peak located above 1 μm can even be achieved. The cavity dependence of the lasing peak provides additional validation of cavity lasing in operation here.

5. Transient spectroscopy measurements

As discussed in the main text, pump fluence dependent TRPL measurements clearly show that the light emission from these CsSnI$_3$ perovskite originates from free carrier recombination (Figure 2). The light emission dominated by trap-assisted mono-molecular recombination at low pump fluence and by free electron-hole bimolecular recombination at high pump fluence. At much higher pump fluence, the charge carrier dynamics will be strongly influenced by the three-particle Auger process. The transition from trap assisted monomolecular recombination to free electron-hole bimolecular recombination is dependent on the unintentionally doped charge carrier concentration. In general, the PL decay dynamics can be described with the following differential equation:[18,34]

$$\frac{dn(t)}{dt} = -k_1 n - k_2 n^2 - k_3 n^3 \tag{S4}$$

where n is the photo-generated charge carrier density, k_1 is the monomolecular recombination rate, k_2 is the bimolecular recombination rate, k_3 is the Auger recombination rate.

Although Figure S4b shows that the Auger recombination lifetime is around hundreds of ps, this lifetime component cannot be accurately resolved when we collect the PL dynamics over a wide time window of 10 ns. Hence, we only fitted the TRPL decay curves (Figure S11 shows the typical ones) with the first and second order decay terms in Eq. S4. The extracted decay rates of the four samples are almost invariant with the pump fluence (below ASE threshold) and are listed in Table S1. It clearly shows that the monomolecular decay rate decreases with increasing the SnF$_2$ concentrations. This suggests that the SnF$_2$-treated samples are of higher quality and have lower carrier-trapping centers compared with the untreated film. However, compared to the leaded CH$_3$NH$_3$PbI$_3$ perovskites with typical 1st order coefficients of 10 μs^{-1} (*i.e.*, ~ 2 orders lower), the SnF$_2$-treated CsSnI$_3$ possess much higher trap densities. However, their bimolecular recombination constants (of ~10^{-8} cm^{3}s^{-1}) are 1-2 orders larger than that of their leaded CH$_3$NH$_3$PbI$_3$ counterparts.[18] Despite the higher trap concentrations, the larger bimolecular recombination constants for these lead-free perovskites could possibly account for their superior gain properties comparable to CH$_3$NH$_3$PbI$_3$. These results clearly suggest that such lead-free CsSnI$_3$ perovskite are more suited for light emitting applications rather than for light harvesting.

Further insights into the carrier recombination mechanisms and the origin of the lasing can be gained from analyzing the transient absorption (TA) spectra and transients (Figure 3, S12-S14). With photon pumping at 1.9 eV (above the band-gap energy), the photo-generated hot charge carriers will cool down to the band edge or trap states within 0.5 ± 0.1 ps (Figure S12).

The band-edge photobleaching (PB) valley (~950 nm) originates from the state-filling of the photo-generated electrons and holes located near the band-edge. The decay of the PB transients arises from electron-hole recombination and/or trapping to the mid-gap trap states as the band edge states becomes depopulated. Note the absence of any obvious PB peak (at 950 nm) for the pristine $CsSnI_3$ film (Figure 3 & S13). Its PB decay therefore originates from the recombination from the trap states. For the SnF_2-treated films, the band-edge PB decay lifetime increases with increasing SnF_2 addition (Figure S14). Assuming a fixed intrinsic electron-hole recombination rate in $CsSnI_3$, the PB lifetime lengthening indicates that the charge carrier trapping from the band edge to the trap states is reduced with the SnF_2 addition. In the $CsSnI_3$ treated films, the PB decay time closely matches the first order PL lifetime (PL lifetime at low pump fluence). For a p-type semiconductor, the PL lifetime is typically limited by the photo-generated electron trapping to the mid-gap states. Hence, this indicates that the band-edge PB peak dynamics is dominated by the state-filling of the electrons. In contrast for the pristine $CsSnI_3$ film, the PB lifetime is much longer than the PL lifetime (Figure S11 & S14), consistent with the earlier interpretation that it originates from a different source (*i.e.*, the recombination from the mid-gap states).

Due to pump fluence dependent transition from trap-assisted monomolecular recombination to free electron-hole bimolecular recombination, the initial time PL intensity ($I_{PL}[t = 0]$) shows a clear transition from linear to quadratic power dependent behavior for the SnF_2 treated $CsSnI_3$ films. Here, contributions of two-photon absorption to the quadratic power dependence is not expected to play a major role as the pump energy (1.9 eV) is much larger than the bandgap of $CsSnI_3$ (1.3 eV).[42] The pump fluences at the transition are determined to be 3.2 ± 0.6, 1.6 ± 0.3 and 0.6 ± 0.1 $\mu J/cm^2$ for the 5%, 10% and 20% SnF_2 added $CsSnI_3$ films, respectively (Figure 2, S17). With linear absorption coefficient of $1.45 \times 10^4/cm$ at 650nm,[27] the corresponding unintentionally doped charge carriers densities are estimated to be ~$1.5 \times 10^{17}/cm^3$, ~$7.6 \times 10^{16}/cm^3$ and ~$2.8 \times 10^{16}/cm^3$. The absence of any linear to quadratic transition for the pristine $CsSnI_3$ film even when pumped with a photo generated charge carrier density as high as $5.7 \times 10^{17}/cm^3$. This result indicates that its doped charge carrier concentration is larger than $5.7 \times 10^{17}/cm^3$.

The dynamical feature of gain in SnF_2 treated $CsSnI_3$ film was also probed with TA. With 650 nm (1 KHz, 50 fs) laser pulse excitation, the light amplification/attenuation of the film was probed by the white-light probe source as a function of time delay. The results are presented in Figure S15 & S16. If we could compare the absorbance before (A_0) and after (A) photon excitation, optical gain is achieved when the photon-induced negative absorbance ($-\Delta A = A_0 - A$) is greater than A_0 (i.e., $\Delta A + A < 0$). However, due to the imperfect morphology of the films (Figure S3), we could not accurately determine the linear absorbance. Nonetheless, by measuring the steady state PL simultaneously with the TA measurement, we can still identify the ASE onset when pumping above the ASE threshold fluence. Figure S15 plots the values of ΔA probed near the band gap under weak and strong fluence excitation, respectively. The PB feature around 950 nm, where the ASE occurs, becomes profound with increasing excitation fluence in the SnF_2 treated films. In untreated film, the PB increasing around 950nm is greatly reduced by photon-induced absorption (PIA). The occurrence of optical gain could be identified as an additional ultrafast process appearing at a time delay of ~0.5 ps upon pumping the SnF_2-treated $CsSnI_3$ films with above threshold fluence (Figure S16b). The lifetime with gain increases with increasing pump fluence. The gain lifetime is around 20 ps when the pump fluence is increased to 80 $\mu J/cm^2$.

6. Temperature dependence of the SE and ASE

Temperature dependent PL measurements afford us an additional means to recheck the recombination mechanisms of SE and subsequently that of ASE in these SnF_2-treated $CsSnI_3$ perovskites. Figure S18**a** shows the evolution of the steady state spectra as a function of temperature following 532nm continuous wave (CW) laser excitation. The PL intensity decreases and the emission peak broadens slightly when the temperature is raised. According to the TRPL measurements (Figure 2, S11 & S17), the photo-induced charge carrier dynamics can be well-described with trap-assisted monomolecular recombination and free electron-hole bimolecular recombination. The band edge light emission originates from the radiative recombination of the free electron-hole plasma. The radiative recombination rate of electron-hole plasma is known to be inversely proportional to the plasma temperature.[43] With the thermally-activated charge carrier trapping and other non-radiative decay channels, the PL intensity will decrease with increasing temperature. The temperature-dependent integrated band edge emission intensities were extracted from Figure S18a and presented in Figure S18b. For the SnF_2-treated $CsSnI_3$ samples, the intensity data can be well-fitted by an Arrhenius plot with one effective thermal activation process:[42]

$$I(T) = \frac{I_0}{1 + A\exp(-E_{ac}/(k_B T))} \tag{S5}$$

where E_{ac} denotes the activation energy for the effective thermal activation process. From the fit, we obtained the effective activation energies of 26 ± 1, 42 ± 2 and 45 ± 2 meV for the 5%, 10% and 20% SnF_2-treated $CsSnI_3$, respectively. Here, this effective thermal activation energy cannot be simply attributed to be the exciton binding energy as this is only applicable for the case of decreasing PL intensity with temperature that is dominated by thermally-induced exciton dissociation. In our case, the PL intensity decrease with increasing temperature could also be attributed to: (i) the thermal-induced reduction of the electron-hole plasma recombination rate; (ii) the thermal-induced charge carrier trapping; or (iii) from some other non-radiative process.

For the pristine $CsSnI_3$, the PL intensity linearly decreases with increasing temperature. The temperature dependent PL curve cannot be fitted using the Arrhenius equation. However, a linear dependence was obtained instead. Such linear dependence could possibly be caused by the extremely high trap density in the untreated sample.

The free electron-hole plasma recombination rate decreases with increasing temperature. With limited trap states density, the increase in the charge carrier recombination lifetime with increasing temperature becomes apparent. By reducing the trap states with SnF_2 treatment, Figure S19 clearly shows that the PL lifetime increases with increasing temperatures for the 10% and 20% SnF_2-treated $CsSnI_3$ samples. Such phenomena is contrary to that commonly observed in semiconductors with excitonic type luminescence.[1-7,42]

The ASE F_{Thr} was measured as a function of temperature for all the SnF_2 treated samples (Figure S20). The results clearly show that F_{Thr} increases with increasing temperature for all the treated samples. This kind of threshold fluence increasing could be partly attributed to the reduced free electron-hole recombination rate with temperature.

7. Stability test

Even with the worst sample (5% SnF_2 treated $CsSnI_3$) in this tin-based perovskite family, the photo-stability of the film is very good (Figure 4a). The coherent light emission properties of the 20% SnF_2 treated $CsSnI_3$ is better than that of the 5% SnF_2-treated $CsSnI_3$. Correspondingly, the photo-stability of the 20% SnF_2 treated $CsSnI_3$ is also very good - Figure S21.

## 8. Theoretical prediction of the coherent light emission wavelength tunability

The atomic and electronic structure of $CsSnBr_xI_{3-x}$ (x = 0, 1, 2, 3) compounds were calculated employing density-functional-theory (DFT) calculations, using the Perdew-Burke-Ernzerhof (PBE96)[44] exchange-correlation potential, and the projector-augment wave (PAW) method,[45,46] as implemented in the Vienna ab-initio simulation program (VASP).[47] In these calculations Cs 5s5p6s, Sn 4d5s5p, I 5s5p and Br 4s4p orbitals were treated as valence states, employing the PAW potentials labeled "Cs_sv", "Sn_d", "I" and "Br" in the VASP PBE library. Four compositions were modeled: $CsSnBr_xI_{3-x}$, where x = 0, 1, 2, 3. For x = 0 and 1, orthorhombic structures were used, and for x = 2 and 3, cubic structures were used as input.[48] For x = 1 and 2 the compounds were modeled with a 40-atom supercell, in which the occupation of Br and I on the anion sublattice were chosen randomly, to approximate a disordered structure. All calculations were fully relaxed with respect to cell internal atomic positions, volume and cell shape. We employed 12*12*12, 6*6*6, 4*8*6 and 8*8*6 k-point meshes for $CsSnBr_3$, $CsSnBr_2I$, $CsSnBrI_2$ and $CsSnI_3$, respectively, and a plane-wave cutoff of 520 eV. After the relaxations, the Δ-sol method[49] was employed to compute the band gaps, based on the changes in energy arising when electrons were added or subtracted from the system. In the implementation of the Δ-sol method, we chose N*=68, as recommended for s-p bonded systems and PBE functionals. When calculating the total energies for systems with surplus and deficient electrons, cell shape, volume and internal atomic positions were held fixed. The calculated results are shown in Figure S22. Although the Δ-sol calculated bandgaps were found to be uniformly larger than the experimental values, both the experimental and theoretical results show a consistent trend of decreasing bandgap with decreasing iodine concentration. These theoretical data further confirm that the wavelength tuning arises from the partial halide substitution and not due to a mixture of phases.
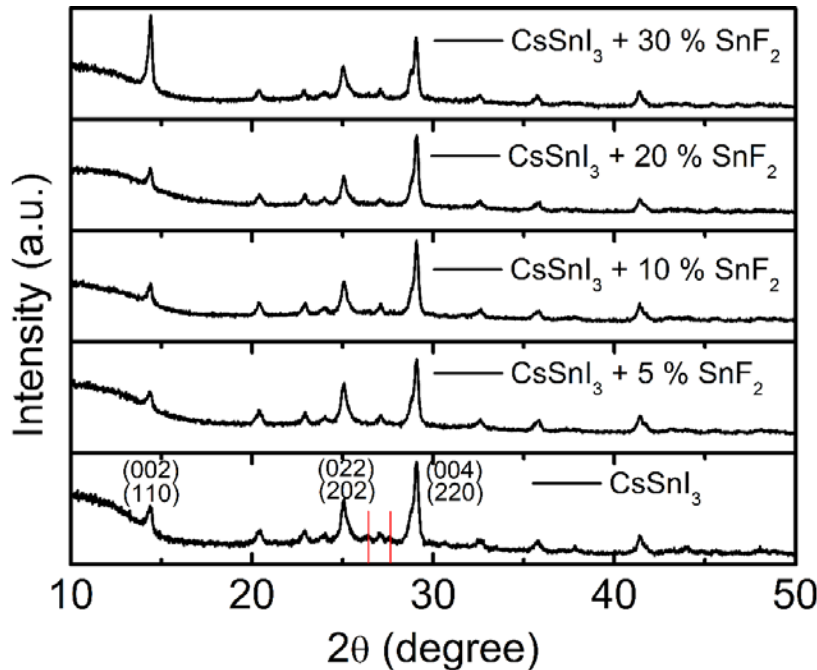
Figure. S1. XRD characterization. XRD spectra of $CsSnI_3$ thin films treated with different concentration SnF_2 on quartz substrates. The peaks are assigned to orthorhombic (Pnam) $CsSnI_3$. The two weak peaks originated from non-orthorhombic perovskite phase in pristine $CsSnI_3$ are totally eliminated with SnF_2 doping.
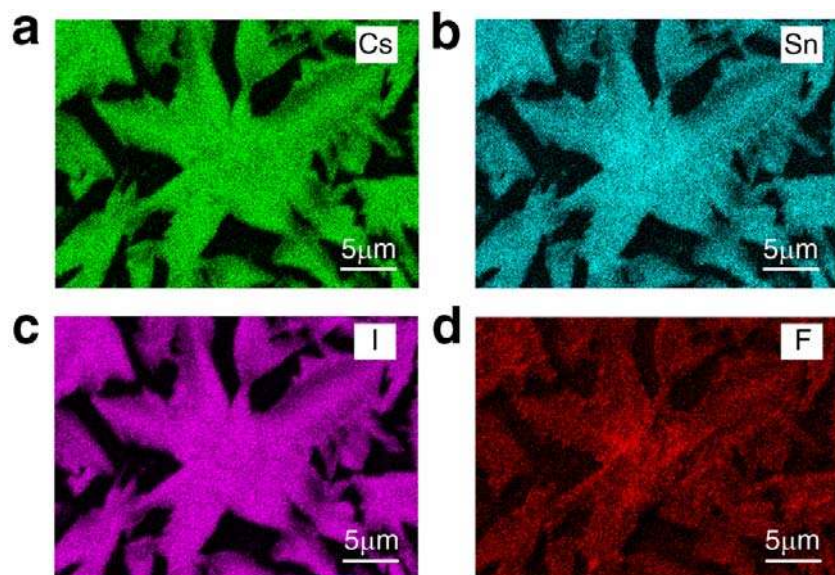
Figure S2. Elemental mapping of the SnF_2-treated Sn-based perovskite. Typical SEM EDX mapping shows the distributions of Cs (**a**), Sn (**b**), I (**c**) and F (**d**) in the 10% SnF_2-treated $CsSnI_3$ film.
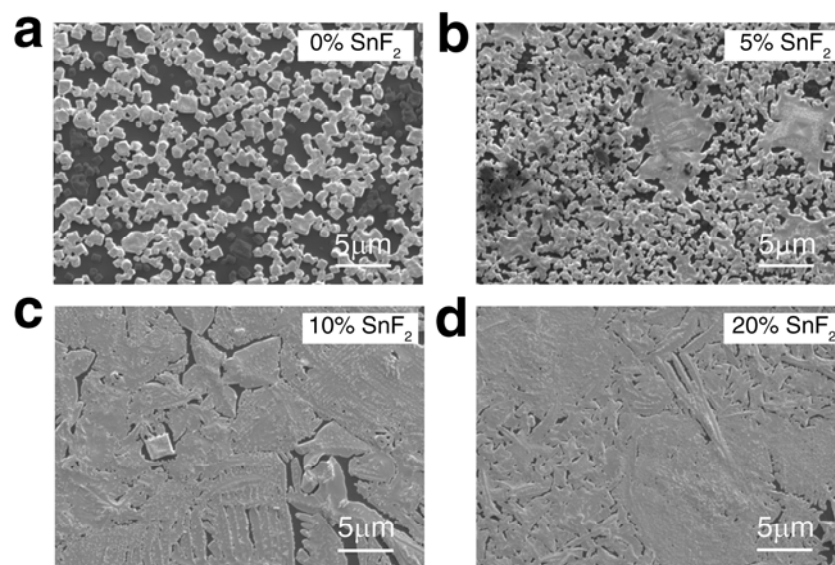

Figure S3. Film morphology characterization of the Sn-based perovskites. Typical SEM images showing the morphology of $CsSnI_3$ films spin-coated from the precursor solutions with 0% (**a**), 5% (**b**), 10% (**c**) and 20% (**d**) SnF_2 addition.
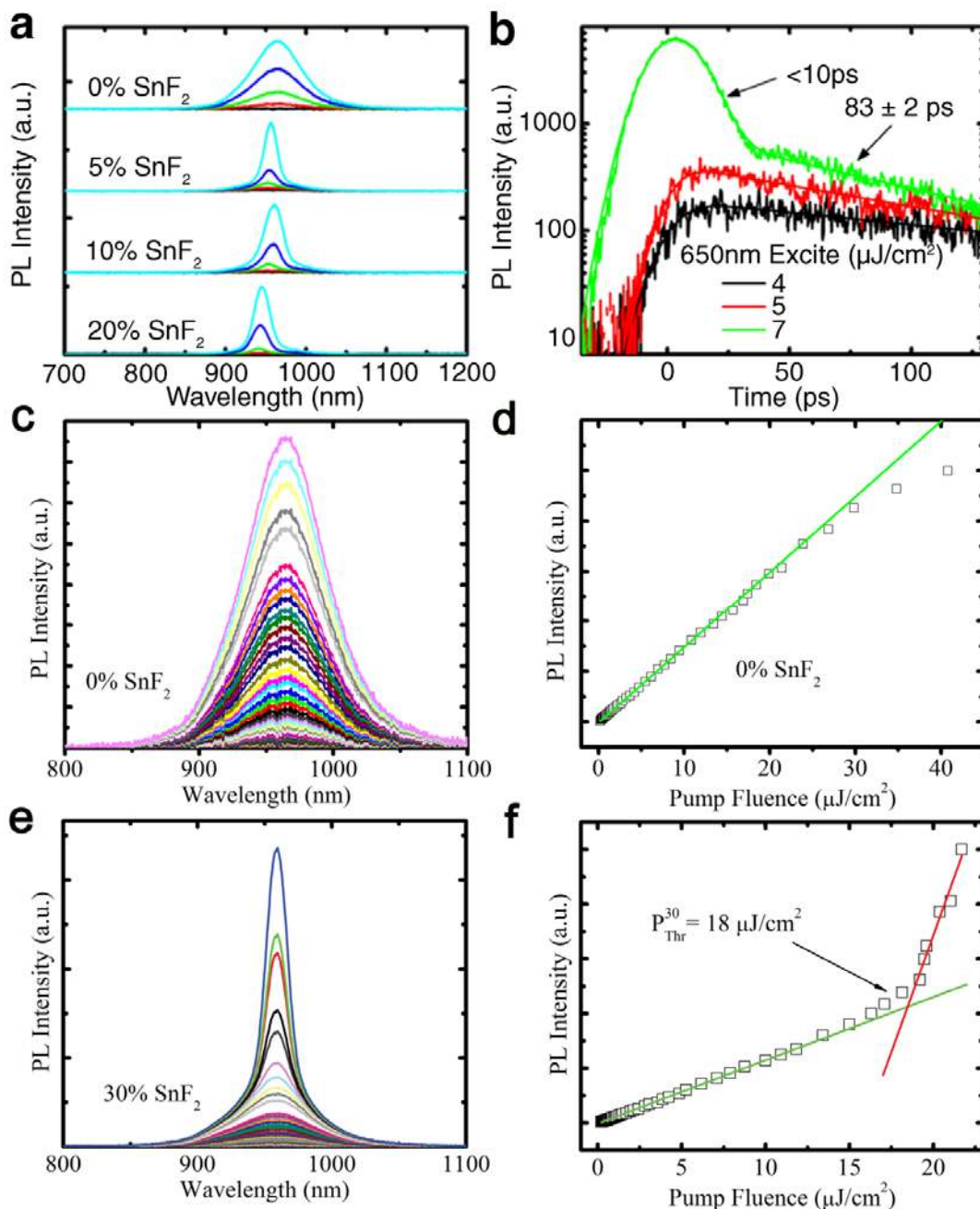
Figure S4. Pump fluence dependent PL and TRPL spectra. a) Steady-state PL emission spectra from the CsSnI$_3$ thin films (with various concentrations of SnF$_2$ added). The plots show the transition from SE to ASE in the SnF$_2$-treated samples, but only SE in the untreated film. The samples were photoexcited using 650 nm laser pulses (50 fs, 1 KHz) with increasing pump fluence. b) Typical TRPL decay transients of the CsSnI$_3$ film with 20% SnF$_2$ addition following photo-excitation with pump fluence below (black and red) and above (green) the ASE threshold. Pump fluence dependent emission spectra for the 0% (c) and 30% (e) SnF$_2$-treated CsSnI$_3$ films. Emission intensity as a function of pump fluence for the 0% (d) and 30% (f) SnF$_2$-treated CsSnI$_3$ films.
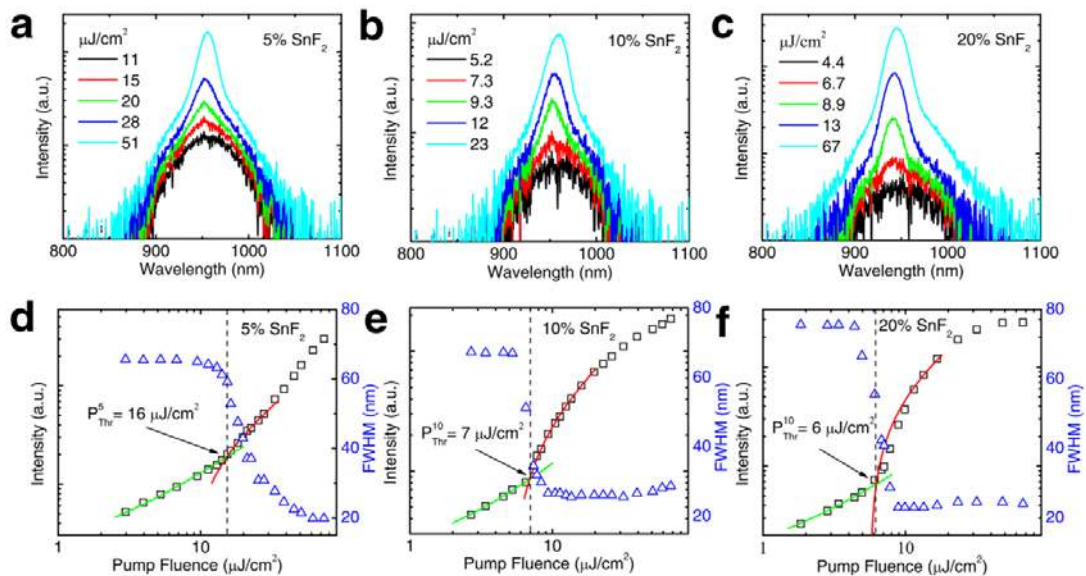
Figure S5. ASE threshold determination. **(a)** – **(c)** Steady state emission spectra showing the transition from SE to ASE. **(d)** – **(f)**, Emission intensity and FWHM as a function of pump fluence above the ASE threshold. The ASE threshold is determined from the intersection of the SE power dependent fit with the ASE power dependent fit.
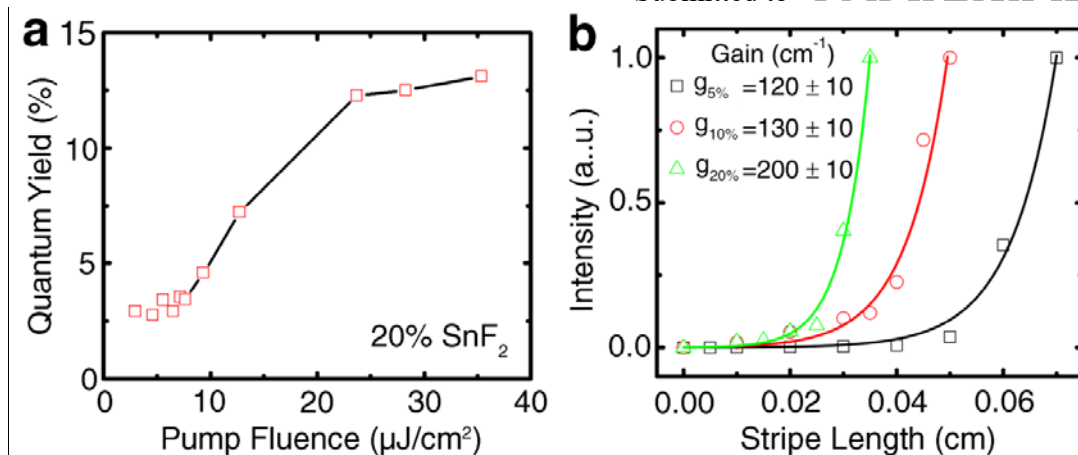
Figure S6. PLQY and Gain Measurements. **a)** Room temperature PLQY measurements of 20% SnF_2-treated $CsSnI_3$ film at various pump fluence. **b)** VSL measurements of the SnF_2-treated $CsSnI_3$ films at a pump fluence of 20 $\mu J/cm^2$. The experiments were conducted with 650 nm pump pulses (50 fs, 1 KHz).
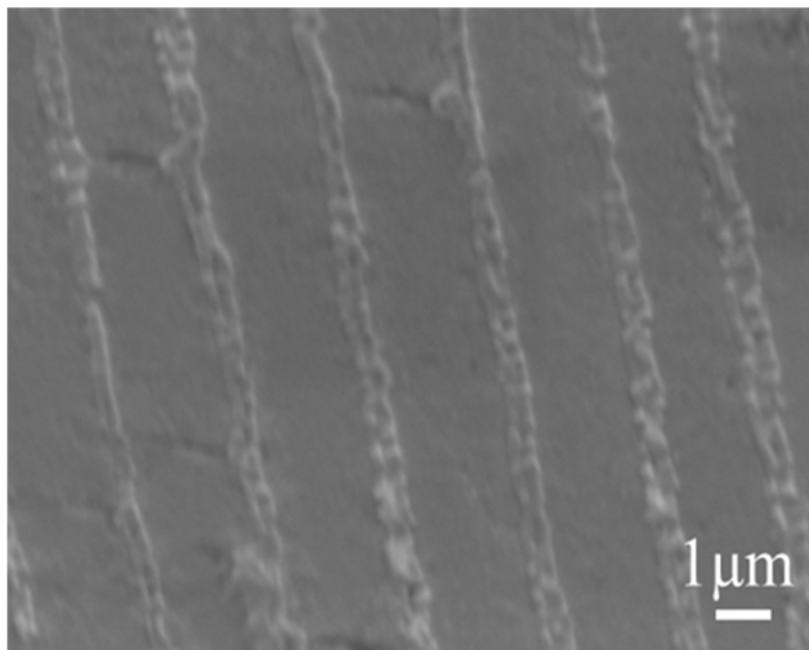
Figure. S7. SEM image showing the infiltration of perovskite into the butterfly wing. The typical SEM image shows that the 20% SnF_2-treated $CsSnI_3$ can infiltrate well into the butterfly wing.
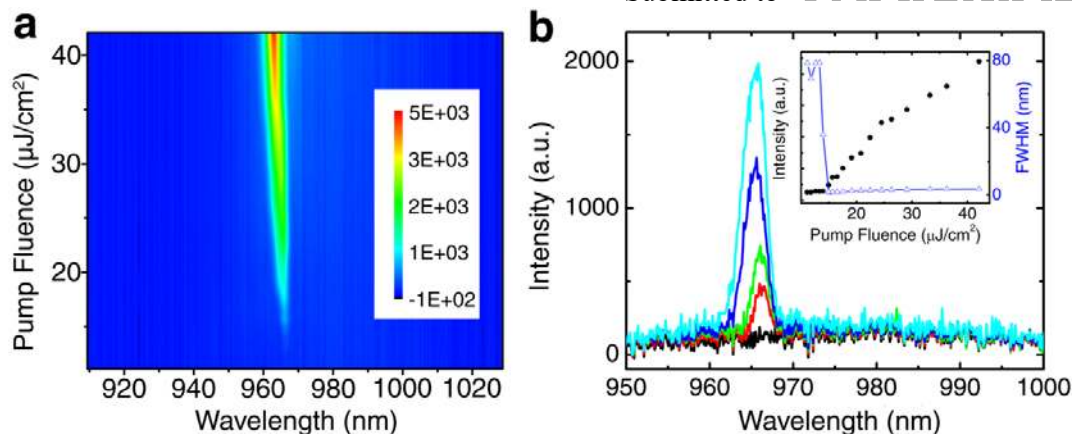
Figure S8. Single mode lasing from lead-free perovskite. **a)** 2D pseudo-colour plot of the single model lasing emission spectra from the butterfly wing embedded with 20% SnF$_2$-treated CsSnI$_3$ as a function of pump fluence. **b**) Emission spectra at various pump fluence extracted from (**a**). Inset: Emission intensity and FWHM as a function of pump fluence showing the lasing threshold at ~15 μJ/cm^2 – also extracted from (**a**).
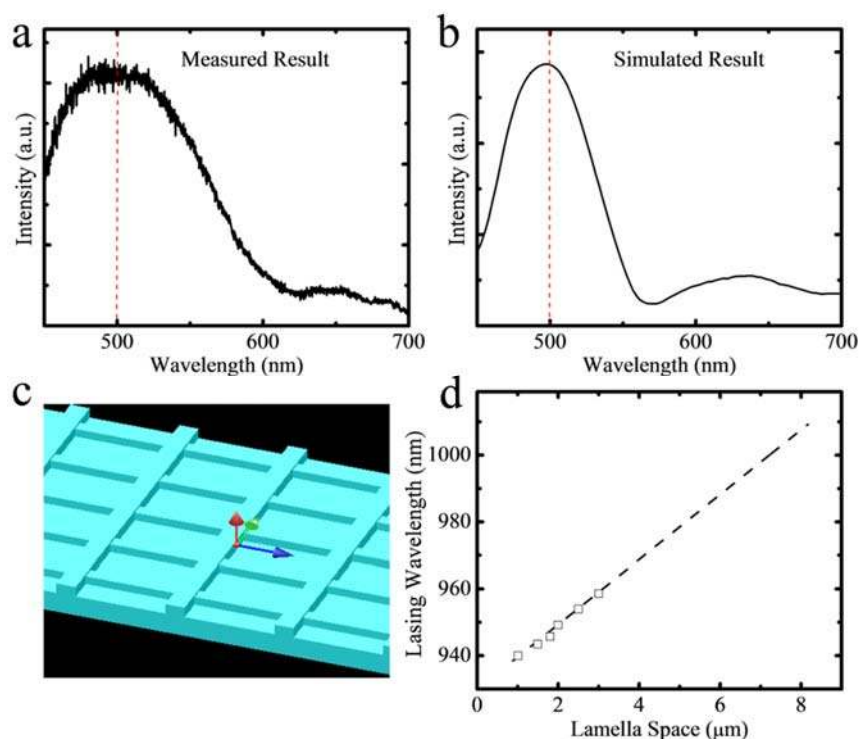
Figure S9. Simulation of the Scattering spectrum of a butterfly wing. **a)** The measured white light scattering spectrum from white area of the butterfly wing. **b)** The simulated scattering spectrum with the FDTD method. Though optimizing the effective refractive index of the butterfly wing, good correspondence between the measurements in (**a**) and the simulation results in (**b**). The red line is a guide to show the scattering spectrum peak position. **c)** A schematic of the structure used for the simulation. **d)** The simulated dependence of lasing peak on the lamella interspacing.
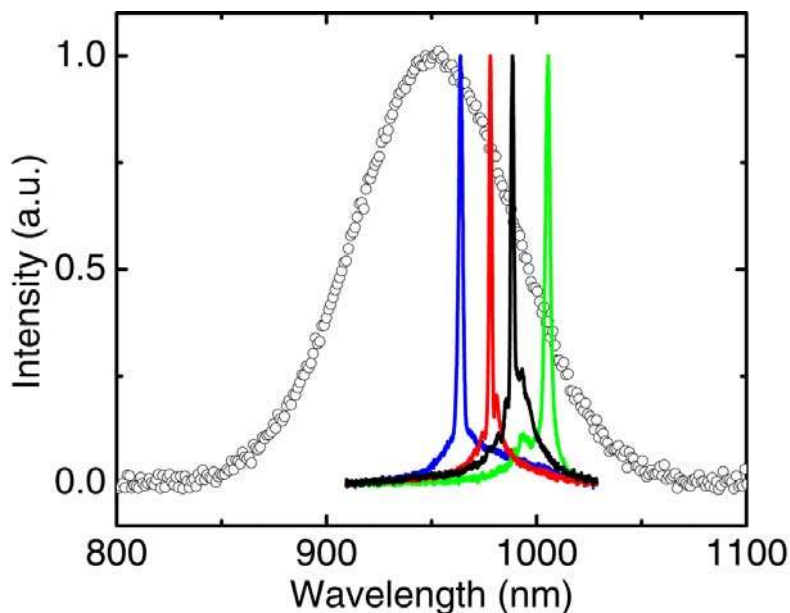
Figure. S10. Tunable lasing from 20% SnF_2-treated $CsSnI_3$ on a butterfly wing. Widely tunable lasing emission (sharp peaks) could be achieved with different cavity size (lamella interspacing) on the different locations of the butterfly wing with 20% SnF_2-treated $CsSnI_3$. The open circle spectrum is the broad PL spectrum. The optical excitation was performed with 650 nm pump pulses (50fs, 1 KHz).
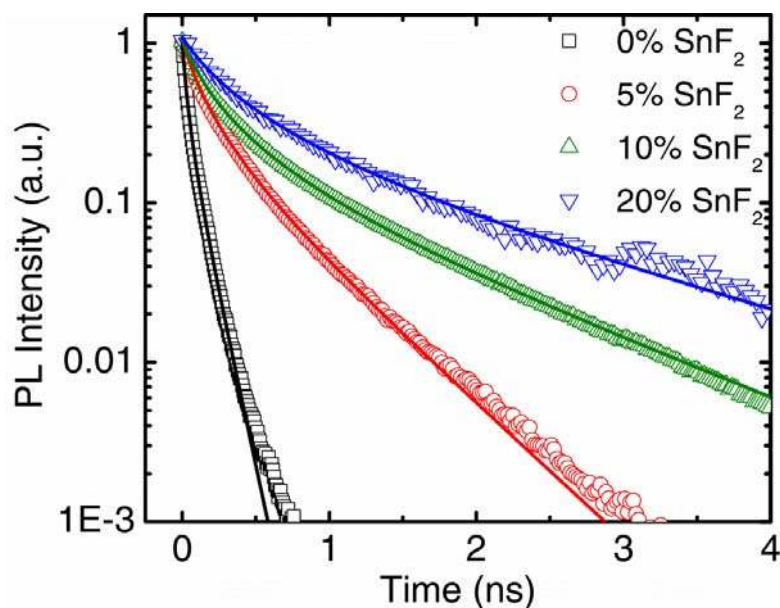

Figure. S11. Transient PL dynamics. Typical TRPL decay transients of $CsSnI_3$ films with SnF_2 addition (integrated over the spectrum) following 650 nm pulses (1 KHz, 50 fs, ~4 $\mu J/cm^2$) excitation at room temperature. Solid lines represent fits with first and second order decay functions.

14
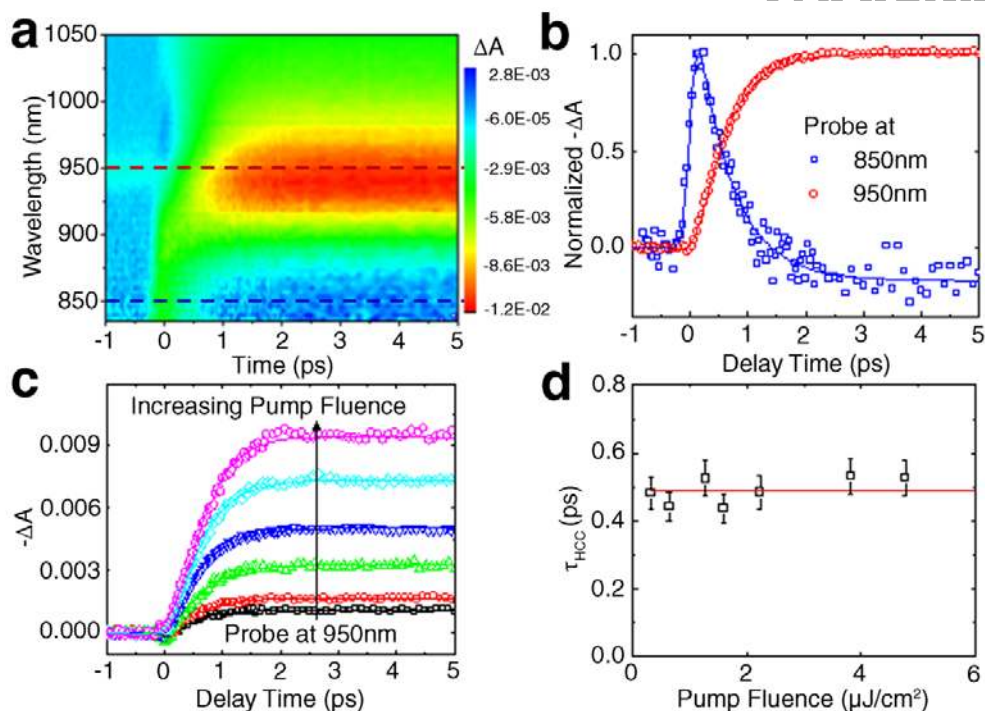
Figure S12. Early time TA dynamics. **a)** 2D TA image shown in short time scale. **b)** PB dynamics at 850 nm and 950 nm as indicated with the blue and red lines in **a** shows the hot charge carrier cooling process. **c)** shows the pump fluence dependent early time dynamics of PB at 950 nm. The extracted hot charge carrier cooling time is shown in **(d)**. The experiments were conducted with 20% SnF_2-treated $CsSnI_3$ following 650 nm laser pulses (1 KHz, 50 fs) excitation.
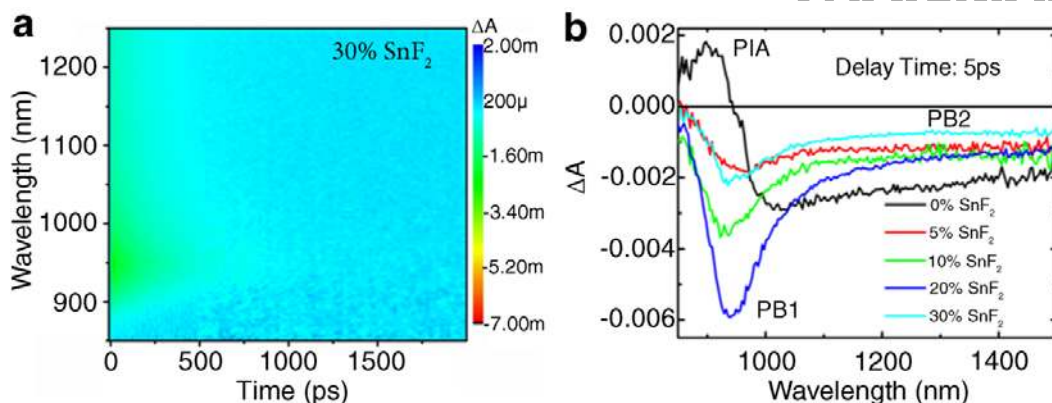
Figure S13. TA spectra. **a)** A pseudo color TA image showing the change in absorption (ΔA) versus probe wavelength and probe delay time for the 30% SnF_2-treated $CsSnI_3$ film. **b)** TA spectra of $CsSnI_3$ thin films treated with different SnF_2 concentrations at 5 ps probe delay time. The TA spectra shown in Figure 3(b) in the main manuscript are replotted with that for the 30% SnF_2-treated sample for clear comparison. The PB feature decreases when the SnF_2 concentration is increased to 30%. These results show that 20% SnF_2 treatment is close to the optimal conditions for treating the $CsSnI_3$ film. The experiments were conducted with 650 nm pump pulses (1 KHz, 50 fs, $\sim$2 $\mu J/cm^2$).
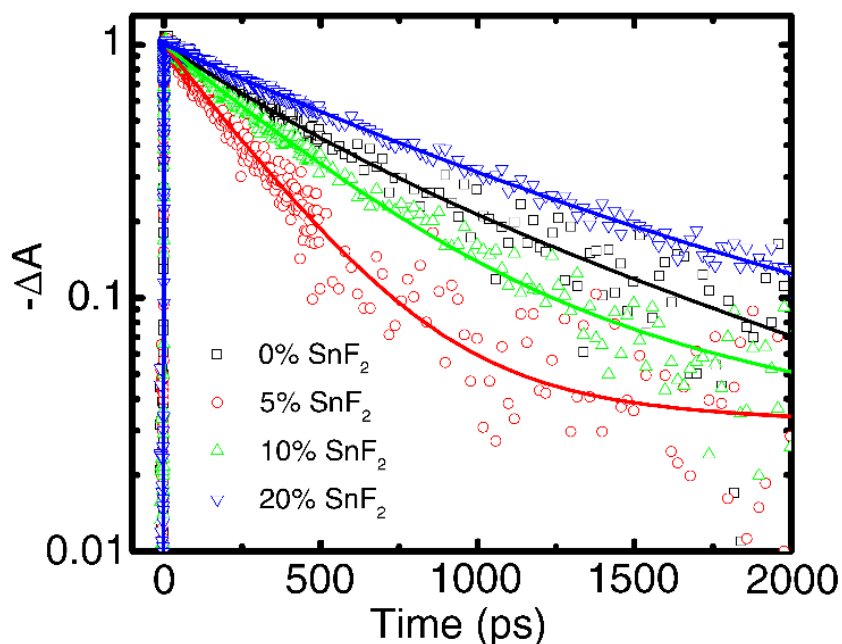

Figure. S14. TA decay dynamics. Normalized bleaching kinetics at 950 nm for the SnF_2-treated $CsSnI_3$ films in an optical cryostat under vacuum following excitation at 650 nm (1 KHz, 50 fs, $\sim$2 $\mu J/cm^2$).
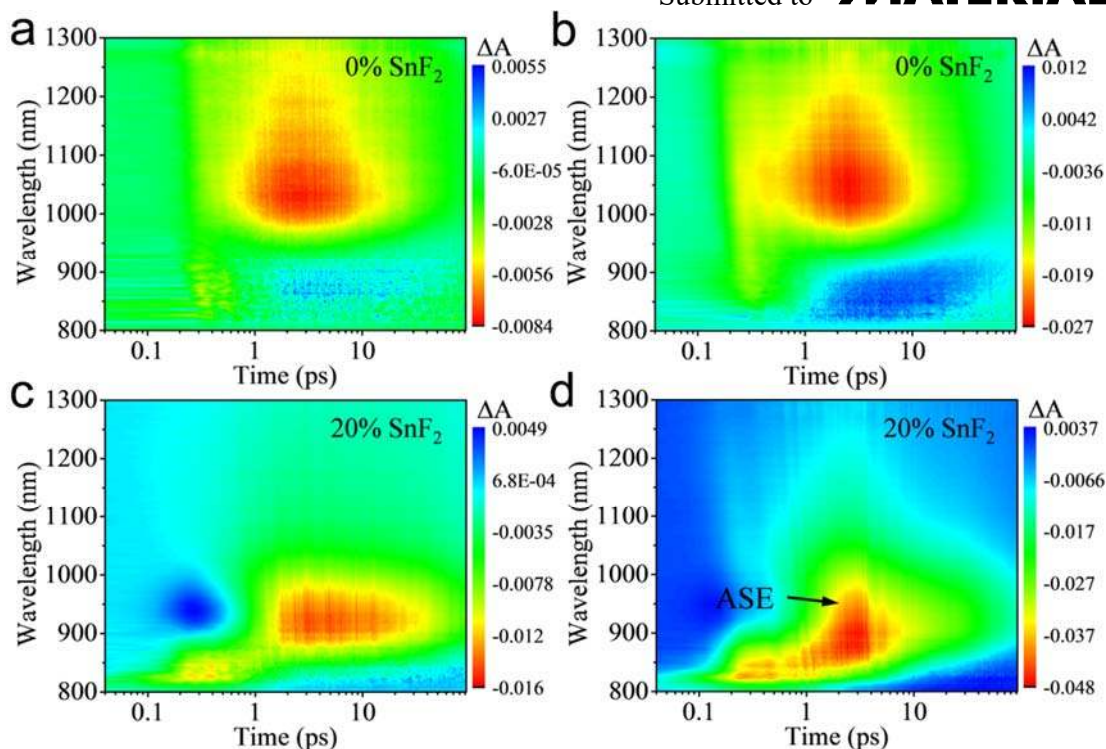
Figure. S15. TA study of optical gain. TA spectroscopic data of the 0% and 20% SnF$_2$ treated CsSnI$_3$ films with 650 nm (1 KHz, 50 fs) laser pulse excitation at ~4 μJcm^{-2} (**a**, **c**) and ~20 μJcm^{-2} (**b**, **d**), respectively. The ASE feature manifests as a pronounced bleach signal upon pumping at high fluence as shown in (**d**).
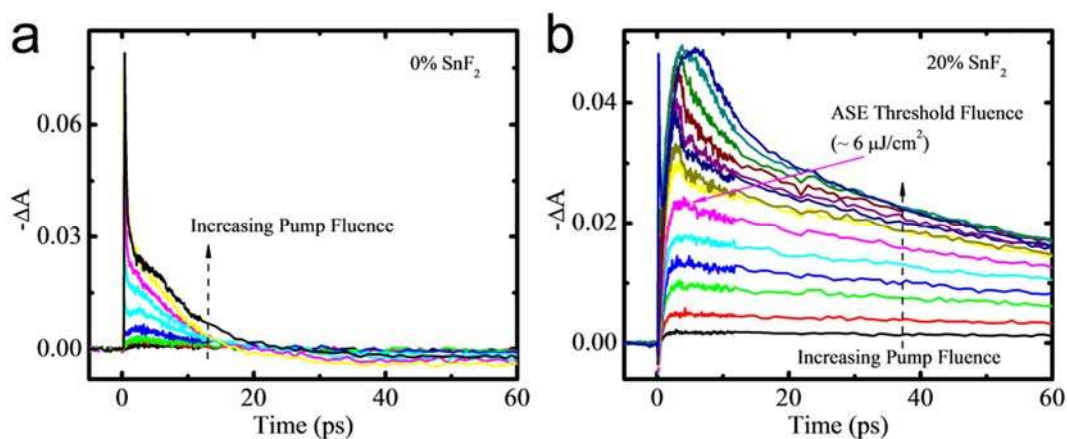

Figure. S16. TA study of optical gain. Pump-fluence-dependent nonlinear absorbance changes (-ΔA) measured at 950 nm. The occurrence of optical gain could be identified as an additional ultrafast process appearing at a time delay of ~0.5 ps upon pumping the SnF$_2$-treated CsSnI$_3$ films with above threshold fluence. The lifetime with gain increases with increasing pump fluence.
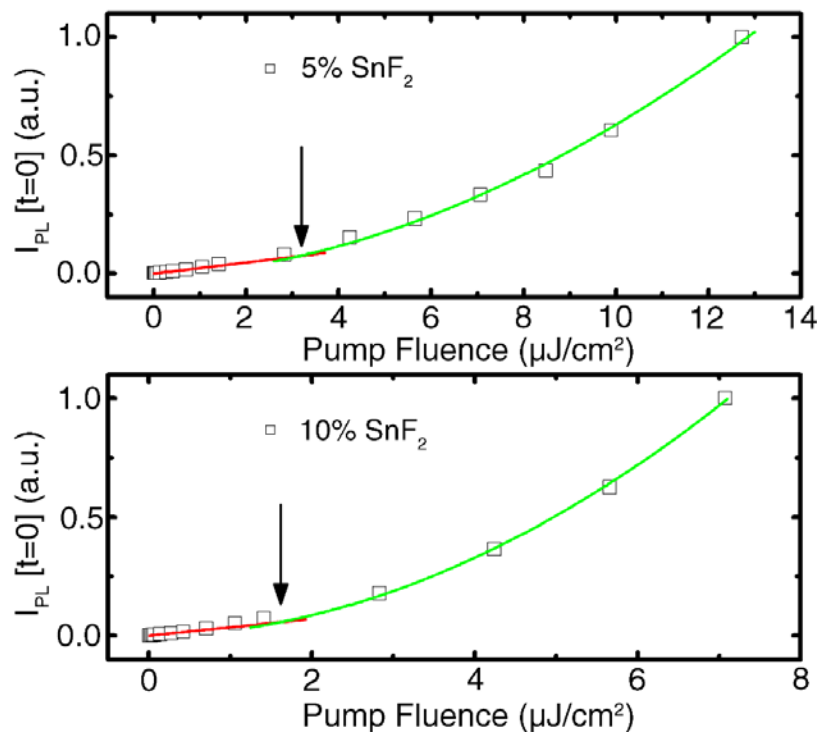
Figure. S17. Pump fluence dependent transient PL intensity. Pump fluence dependence of the initial time PL intensity $I_{PL}(0)$ for the 5%, and 10% SnF$_2$-added CsSnI$_3$. The experiments were conducted with 650 nm laser pulses (1 KHz, 50 fs). The intersection between the linear fit (red line) and the quadratic fit (green curve) yields an estimate of the doped carrier densities.
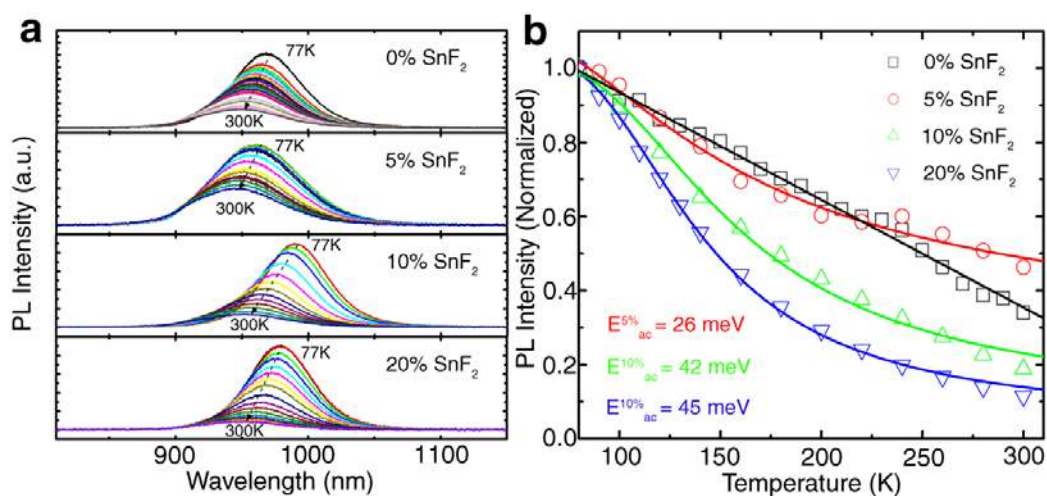
Figure S18. Temperature dependence of PL. **a**) PL spectra from 77 to 300 K for the SnF$_2$-treated CsSnI$_3$. **b**) Integrated PL intensity as a function of temperature. For the SnF$_2$-added samples, the solid lines are the fittings with effective thermal induced charge carrier trapping theory. For the untreated CsSnI$_3$, the solid line is a simple linear fit intended as a guide for the eye.
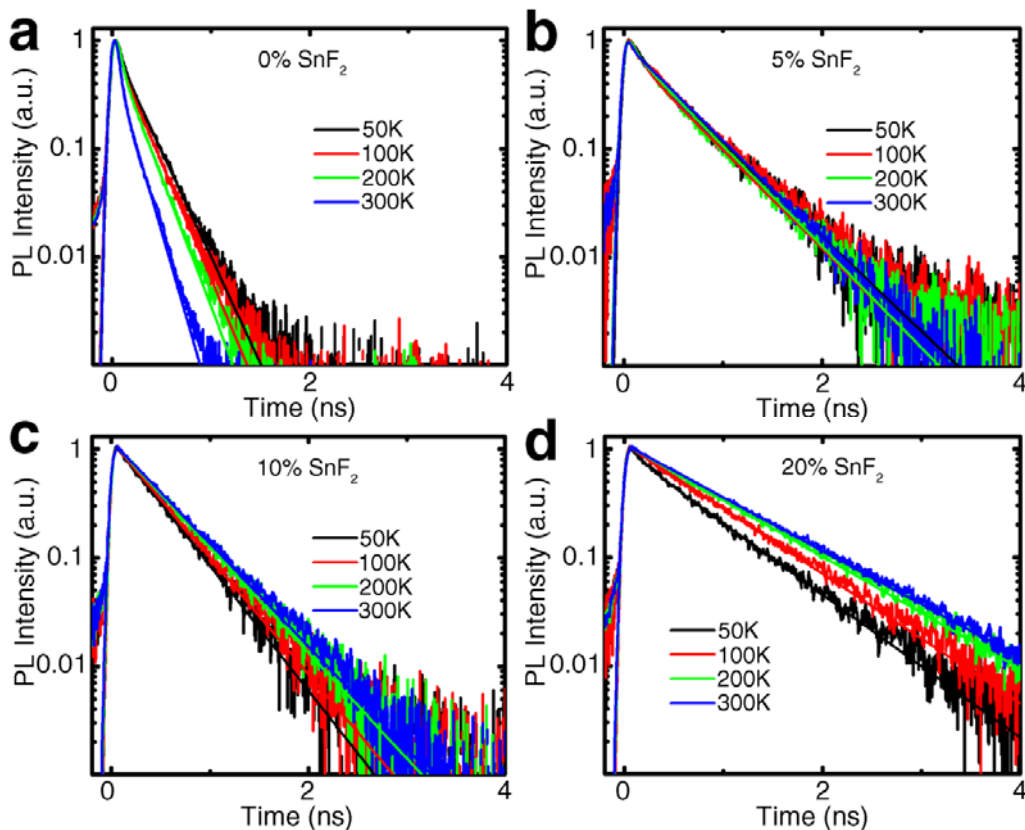
Figure S19. Temperature dependences of transient PL dynamics. Time-resolved PL decay transients for the SnF$_2$-treated CsSnI$_3$ perovskites (integrated over the spectrum) following 650 nm pulses (1 KHz, 50 fs, ~1 µJ/cm^2) excitation at different temperatures. With increasing temperatures, the PL recombination lifetimes increases for the 10% and 20% SnF$_2$-treated CsSnI$_3$.
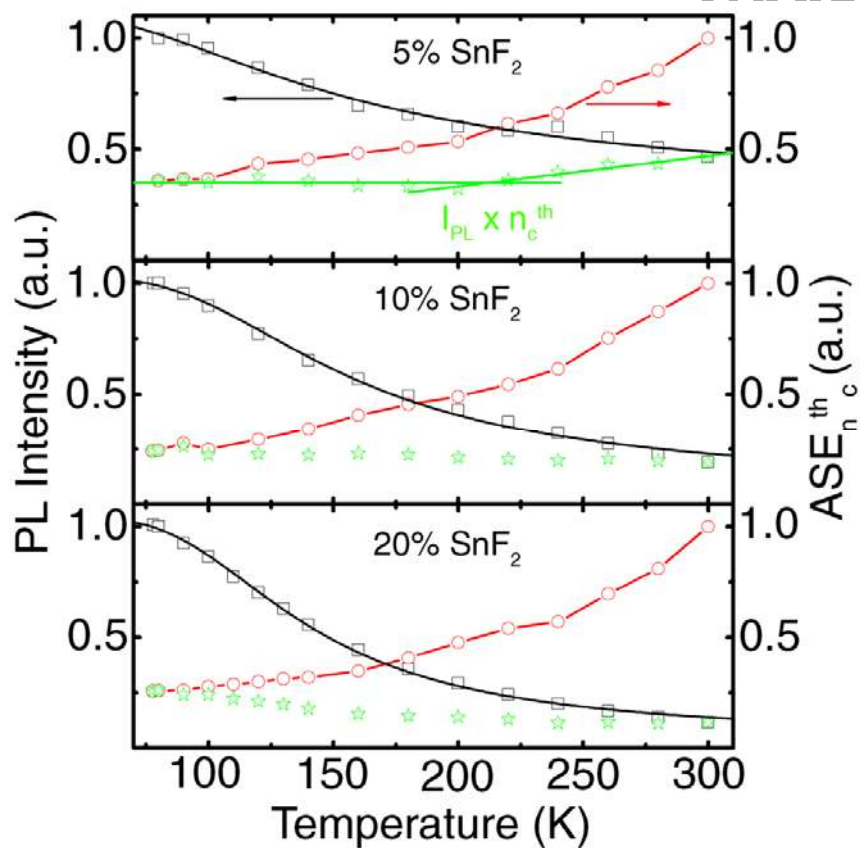
Figure. S20. Temperature dependence of the ASE thresholds. Normalized temperature dependent ASE thresholds (red circles), normalized temperature dependent PL intensities when fixed the pump fluence (black squares). The green stars are the products of the ASE thresholds and the relative PL intensities. The ASE characterization is conducted with 650 nm laser pulses (1 KHz, 50 fs).
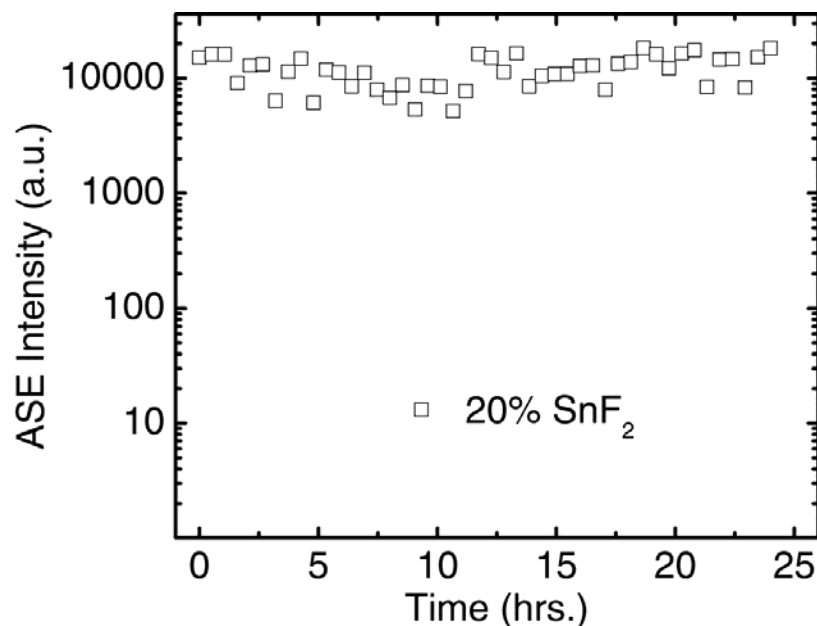
Figure. S21. Stability test. Time-dependent ASE intensity of the 20% SnF_2-treated $CsSnI_3$ film with a pump fluence of 30 $\mu J/cm^2$ (650 nm, 50 fs, 1 KHz).
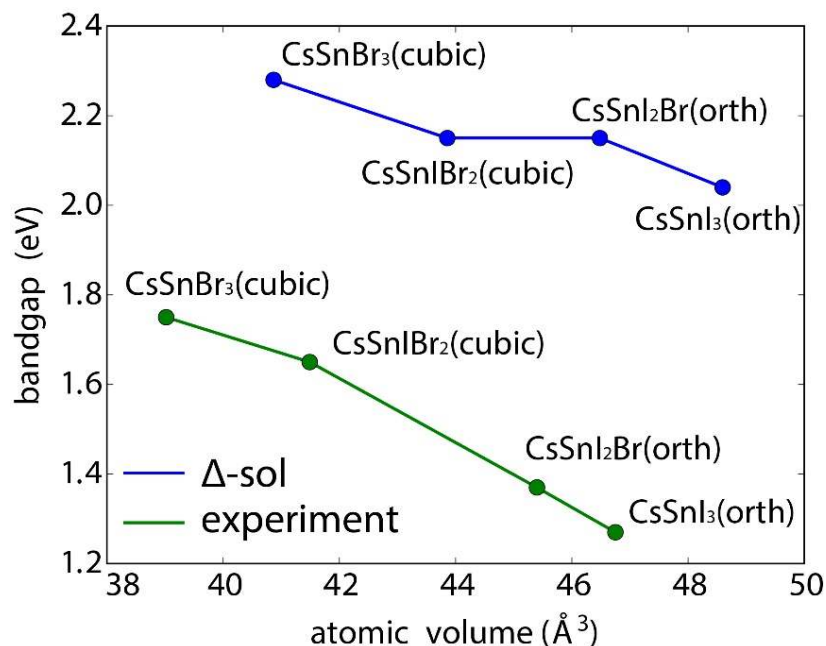
Figure. S22. Calculated band gap tunability of the $CsSnBr_xI_{3-x}$. Theoretical predicted band gaps of $CsSnBr_3$, $CsSnBr_2I$, $CsSnBrI_2$ and $CsSnI_3$ with the Δ-sol method. The experimental results were also plotted here for comparing the trend of the bandgap tuning.

Table S1. Charge-carrier decay rates of $CsSnI_3$ with SnF_2 addition in different concentration.

CsSnI$_3$ with	0% SnF$_2$	5% SnF$_2$	10% SnF$_2$	20% SnF$_2$
1st order [μs^{-1}]	1.3 ($\pm$ 0.4) $\times 10^4$	2.4 ($\pm$ 0.7) $\times 10^3$	1.1 ($\pm$ 0.3) $\times 10^3$	7 ($\pm$ 2) $\times 10^2$
2nd order [cm^{3}s^{-1}]	6 ($\pm$ 2) $\times 10^{-8}$	1.7 ($\pm$ 0.5) $\times 10^{-8}$	1.5 ($\pm$ 0.4) $\times 10^{-8}$	1.0 ($\pm$ 0.3) $\times 10^{-8}$

References and Notes:

38.   N. Dutta, R. Nelson, *J. Appl. Phys.* **1982**, *53*, 74-92.
39.   K. L. Shaklee, R. F. Leheny, *Appl. Phys. Lett.* **1971**, *18*, 475.
40.   J. Huang, X. Wang, Z. L. Wang, *Nano Lett.* **2006**, *6*, 2325.
41.   Hayatullah, G. Murtaza, S. Muhammad, S. Naeem, M. N. Khalid, A. Manzar, *Acta. Phys. Pol. A* **2013**, *124*, 102.
42.   G. Xing, J. Luo, H. Li, B. Wu, X. Liu, C. H. A. Huan, H. J. Fan, T. C. Sum, *Adv. Opt. Mater.* **2013**, *1*, 319.
43.   G. Bongiovanni, J. L. Staehli, *Phys. Rev. B* **1992**, 46, 9861.
44.   J. P. Perdew, K. Burke, M. Ernzerhof, *Phys. Rev. Lett.* **1996**, *77*, 3865.
45.   P. E. Blöchl, *Phys. Rev. B* **1994**, 50. 17953.
46.   G. Kresse, D. Joubert, *Phys. Rev. B* **1999**, *59*, 1758.
47.   G. Kresse, J. Furthmüller, *Phys. Rev. B* **1996**, *54*, 11169.
48.   D. Sabba, H. K. Mulmudi, R. R. Prabhakar, T. Krishnamoorthy, T. Baikie, P. P. Boix, S. Mhaisalkar, N. Mathews, *J. Phys. Chem. C* **2015**, *119*, 1763.
49.   M. K. Y. Chan, G. Ceder, *Phys. Rev. Lett.* **2010**, *105*, 196403.